PREPRINT

This is a non-peer reviewed preprint submitted to EarthArXiv

Contextual learning improves forest above-ground biomass estimates from UAV-LiDAR: use of tree trait associations.

Jaime C. Revenga[1] | Stefan Oehmcke[2] | Mana Gharun[3] | Flurin Sutter[4] | Katerina Trepekli[1] | Fabian Gieseke[2] | Nina Buchmann[5] | Alexander Damm[6,7]

[1]Institute of Geosciences and Natural Resources Management (IGN), Copenhagen University Denmark

[2]Institute of Computer Science (DIKU), Copenhagen University, Denmark

[3]Institute of Landscape Ecology, Biosphere-Atmosphere Interaction, University of Münster, Germany

[4]Swiss Federal Institute for Forest, Snow and Landscape Research (WSL), Forest Dynamics Research Unit, Switzerland

[5]Department of Environmental Systems Science, ETH Zürich, Switzerland

[6]Department of Geography, University of Zürich, Winterthurerstrasse 190, 8057 Zurich, Switzerland

[7]Eawag, Swiss Federal Institute of Aquatic Science & Technology, Surface Waters – Research and Management, Ueberlandstrasse 133, 8600 Duebendorf, Switzerland

Correspondence
Jaime C. Revenga, Institute of Geosciences and Natural Resources Management (IGN), Copenhagen University, 1350, Copenhagen, Denmark
Email: jar@ign.ku.dk

Funding information

Forest structure analyses and biomass prediction systems are key tools for advancing forest trait-based ecology and ecosystem stewardship. The combination of near-field remote sensing techniques—e.g., Unmanned Aerial Vehicles (UAV) and Light Detection and Ranging (LiDAR) systems—with machine-learning methods enhances the accuracy of forest structure analyses and above ground-biomass (AGB) estimates. In this study, we utilized a UAV-LiDAR system to map the 3D architecture of a monoculture Norway spruce forest in Davos, Switzerland, where a field-based inventory served as ground truth data. The objectives of this effort were (i) to gain insights into variation and gradients of structural traits (i.e., tree height) and (ii) to evaluate whether this knowledge of community structure may prove useful as contextual information to improve predictions of AGB at the individual tree level. To investigate the local association of structural traits, we segmented the point cloud data scene into individual trees and treated tree height as the morphological variable of interest. We then used local indicators of spatial association to determine the extent of significant local context, and defined tree neighborhoods within the forest. For the task of AGB regression, we obtained results of several feature-based regression methods (i.e., AdaBoost, Lasso and Random Forest) and evaluated these based on nested cross-validation.

We applied this approach to two separate tree data sets within the same site, one being clustered and continuous, the other discontinuous and scattered in separate sampling plots. In both cases, we found evidence of enhanced AGB prediction performance in context-aware regressions, indicating that gradients in morphological tree traits across the ecosystem proxy for unveiled ecological information that influence tree growth, which can be leveraged to enhance predictions of AGB.

KEYWORDS

above-ground biomass, forest structure, functional trait mapping, machine learning, contextual learning, UAV-LiDAR, quantitative ecology

---

---

1 | INTRODUCTION

Above-ground biomass (AGB) is a critical component for determining global land carbon (C) budgets. Worldwide, forests are critical agents of the global C-cycle, as major sinks of atmospheric carbon dioxide [1, 2]. However, current estimates of C-cycling from land ecosystems have large margins of uncertainty, partly because of uncertainties in AGB estimates [3]. To date, the existence of seemingly equivalent but disparate AGB products hinders a more frequent use of such data products in conservation management [4] or current policy making [5]. Therefore, the growing number of AGB products need to be harmonized and techniques standardized.

Ongoing efforts within the remote sensing (RS) community aim at reducing the uncertainty of AGB predictions to allow reliable estimates across scales [6]. This is a considerable undertaking, since the technology, data sources and methods employed at different scales vary greatly, making it difficult to track propagated errors [6], or to determine how different end-products (i.e., AGB maps) perform comparatively [7]. This lack of standardization results in AGB and trait-mapping products with different degrees of agreement, making it particularly relevant to compare data-acquisition methods [8] and validation procedures [7, 9] of the AGB products [10, 11]. In this scenario, Unmanned Aerial Vehicle (UAV) & Light Detection and Ranging (LiDAR) monitoring systems are regarded as particularly versatile [12], accurate and cost-effective [13] tools to be bridged to regional scale maps seamlessly [6]

Current RS-driven biomass research focuses on algorithmic developments for the detection and segmentation of single trees, in order to enable more precise estimates of structural tree traits [14, 15, 16]. Also, recent reference work analyzing forest structure exploits the use of laser sensors to develop methods for volume reconstruction from point cloud data (PCD) [17, 18]. Furthermore, large-scale AGB mapping initiatives pursue characterizing scale-independent LiDAR-derived predictors to develop LiDAR-to-AGB models across scales [10, 19]. More specifically, in relation to recent advances in forest monitoring using close-range LiDAR technologies the development of versatile, practical and new cost-effective sensors [13] and platforms [20] has seen a rapid growth, widening the applicability of the emerging LiDAR systems [12, 21]. Their emergence has triggered discussions and investigations related to sensor accuracy, sensor types [22] and purpose-adapted surveying methods [23]. However, to date, efficient tree-level phenotyping has been challenged by several forest structural conditions, such as crown-shift [24], canopy closure [25] and tree clumping effects [26, 27].

Traditionally, assessments of tree structural traits from middle- and close-range RS data focused on individual tree attributes as predictors (e.g., tree height, tree canopy metrics) [28]. Over time, methods that consider plot-level metrics to improve the regression of individual tree traits emerged, e.g., non-linear mixed effects (NLME) methods [29, 30, 31], or competition-based methods [32, 33, 34]. In fact, plot-level information has long been reported as beneficial in diverse tree-level assessments, e.g., diameter at breast-height (DBH) [31], surface-based fuel potential [35] or tree height and crown structural metrics [31, 36, 37].

While all these theoretical and technological advances have accelerated the progress of forest biomass research in an unprecedented manner, there is still room for improvement as regards integrating ecological reasoning into biomass research. For instance, scholars argue that understanding local ecological processes requires monitoring biomass of individual trees [14, 33]. However, the opposite idea is seldom discussed: how and to what extent can community ecology processes be harnessed in tree-level AGB regression experiments [32, 34]? We consider this line of work within AGB research as yet relatively unexplored, with some exceptions. Earlier works have proposed to account for the effects of immediate competition pressure on tree growth with either distance-based [34] or distance-independent metrics [38], and judge such approaches beneficial. More recently, Sun et al. (2019) [32] evaluated the potential of distance- and ranking-based competition metrics for improving predictions of tree diameter growth, and found them outperforming competition-unaware prediction models. Similarly, Zhang et al. (2020) [33] ranked trees by quantiles and competition levels to enhance predictions of the tree height-to-diameter ratio.

Despite the utility of current methods that leverage plot-level metrics, they remain unsatisfactory in some respects. Many of such methods are not directly transferable to a RS framework because they use understory metrics as predictors [32, 33]. More importantly, questions remain about the optimal scale at which such metrics should be retrieved. We noticed that, in the reviewed studies, the spatial scale at which ecological phenomena operate was not questioned. Instead, the focus is often on plot-level metrics, measured at an arbitrary distance that corresponds to the size of artificially-bounded forest inventory plots [29, 30, 31, 32, 33]. To the best of our knowledge, tree-level AGB and trait assessments considering context information are currently limited for one or more of the following reasons: (i) they characterize context with uniquely process-specific indices (e.g., competition pressure from immediate neighbors) [32, 33, 34]; (ii) calibrating models with neighbor-metrics retrieved from artificially-bounded inventory plots (e.g., NLME methods) [29, 30, 31]; (iii) they do not sufficiently account for the spatial scale at which the ecological phenomena affect the trait under investigation. Moreover, when the relationship between the plot-level predictors used and the ecological phenomena is described, often ancillary data sources are incorporated (e.g., tree stand age) [33, 39] or non-standardized, forest management terms , e.g.,"stand quality", "site index", "dominance index" [30, 33, 39]. These shortcomings currently hinder the transferability of such methods to other regions, larger scales or different data collection surveys.

Given the need for methods to be scalable and transferable, it certainly appears beneficial to characterize biotic interactions (e.g., tree competition) or environmental filtering (e.g., soil depth, nutrient availability) with metrics that can be remotely sensed such as tree height and crown dimensions, rather than understory predictors, as has been proposed [32].

A central question in community ecology is how functional trait diversity (e.g., the spatial distribution of tree heights) relates to ecosystem dynamics across environmental gradients [40, 41]. In this regard, current AGB research and mapping initiatives [10, 42] have not yet thoroughly investigated the opportunity to consider two-dimensional spatial patterns [43] of remotely-sensed predictors (e.g., tree height, crown dimensions) to enhance tree-level AGB estimations. These predictors, being subject to a concert of spatially continuous ecological factors—e.g., adaptation to different lighting conditions [44, 45] and soil depth variation [46], or the availability of nutrients and nonstructural carbohydrates [47]—exhibit, as a response, local spatial association (i.e., geographical clusters and gradients of similar tree heights) [48]. Such spatial associations of predictors may serve as proxy for the combined effect of the ecological phenomena being considered. Therefore, provided that spatially continuous ecological factors mediate individual tree growth [1, 49]—and these can be remotely sensed—, it seems plausible to use this information about the local context to improve tree-level AGB assessments. In addition, it appears relevant to examine the significance and spatial extent of the local context, as well as the relationship between context-based traits and individual tree traits.

In this framework, machine learning (ML) regression methods seem to be an interesting approach to incorporating a contextual analysis, given that they are commonly integrated into UAV-based forest mapping studies [50]. In such approaches it has been shown that the inclusion of information of local context (i.e., information about the surroundings of the target object) improves their performance [51, 52]. This information can be included in a learning model by either enlarging the receptive field size (i.e., widening the field of view) [53, 54] or by incorporating context-aware features that encode neighboring information into the target object [55] (i.e., a subject tree in our case). In other research fields, such contextual analyses have been successfully incorporated into learning models to improve assessments in, e.g., land-use dynamics [56], Earth system modelling [57] or urban growth [58].

To date, the absence of standardized and scalable approaches to incorporate context information into AGB regression experiments has hindered the potential to harness context to enhancing AGB mapping products. The potential of the spatial association patterns of individual tree traits to represent the effect of local ecological phenomena on tree structure is an area that yet remains partially unexplored in AGB research. Specifically, the question that is still unanswered is how context-awareness can be incorporated into a RS framework and leveraged to enhance AGB estimates at the individual tree level.

In order to address this question, this study aims to evaluate whether AGB regression models can leverage context-awareness to improve AGB estimates at the individual tree level in a mono-culture forest, where the context is defined without using external ancillary data sources, or using neighborhood metrics of artificially-bounded inventory plots. The objectives for achieving this aim include: (i) collecting close-range point cloud data (PCD) via UAV-LiDAR surveying, (ii) retrieving contextual information based on the geographic spatial association of tree heights, (iii) developing methods that allowed the context to be defined and incorporated into regression experiments and (iv) evaluating the effect of introducing context-awareness in tree-level AGB estimates.

2 | MATERIALS AND METHODS

2.1 | Study Area

The Seehornwald Davos research site is located in a managed subalpine coniferous forest on the western flank of the Seehorn mountain, near Davos, in the Swiss Alps (46° 48'55.2 "N, 9° 51'21.3" E, 1640 m a.s.l.). The site is labeled as a class-1 forest ecosystem station of the Integrated Carbon Ecosystem Station (ICOS) network [59] where regular forest inventory measurements are collected following standardized protocols. The site is covered by spruce trees (Picea abies (L.) Karst.) with an average height and age of 18 m and 100 years, respectively, while some trees reach a height of 35m and an age of 300 years. Patchy vegetation (i.e., dwarf shrubs and mosses) covers around 30% of the forest floor. The research site is part of national (LWF[60], TreeNet[61], SwissFluxNet [62]) and international research networks (ICOS [63], ICP Forests [64], eLTER [65]).

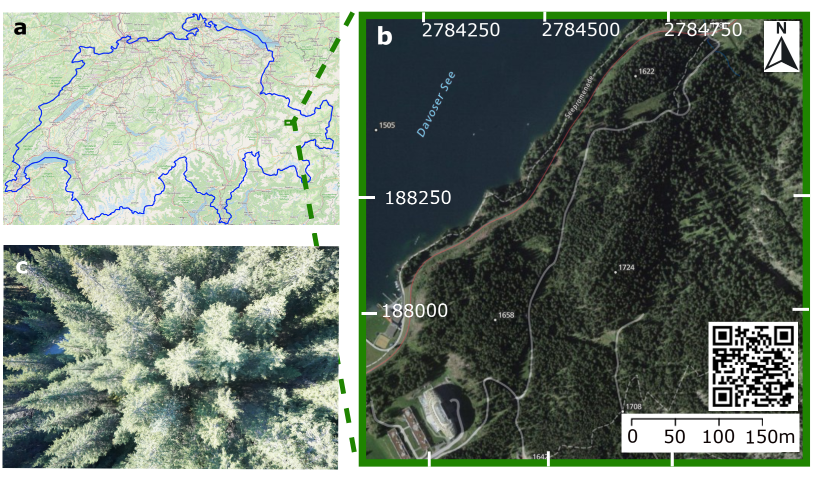

FIGURE 1 **a:** location of the study site; the blue outline delineates the national territory of Switzerland (adapted from open.sourcemap.com). **b:** orthoimage of the study site (adapted from swisstopo.admin.ch); coordinate units are in m, with LV95 as a projected reference system; QR code links to additional information of the study site. **c**: RGB image of forest canopy from a nadir angle taken during the survey.

2.2 | UAV-LiDAR Survey and Field-Based Measurements

We used a UAV-borne LiDAR system mounted to a DJI Matrice 600 Pro payload at a 90° pitch angle, and same heading and roll as the UAV platform. The system included a discrete infrared LiDAR scanner (M8 sensor, Quanenergy Systems, Inc. Sunyvale, CA, USA) and the corresponding state-of-the art inertial and navigation systems. In addition, we used a ground based differential Global Positioning System (dGPS, Trimble R8) during the UAV-LiDAR survey, set up in post-positioning kinematic (PPK) mode, which logged real-time satellite coverage (cf. Ravenga et al. 2022 [66] for details on the airborne and ground system). The coupling of the satellite coverage data with the UAV-based laser and navigation data produced, allowed the generation of georeferenced point clouds, following Davidson et al. (2019) [67].

Data were acquired with a terrain-adapted flight height (Figure 2, a) and 20% overlap between individual LiDAR scans of ca. 50 m width and 250 points/m^2 (cf. Revenga et al. 2022 [66] for additonal details on applied flight parameters). The surveys were conducted in October 2021, coinciding with the end of the growing season. Figure 2 (a) shows the trajectories of the individual UAV-LiDAR flights during the survey campaign. While the standard survey coverage followed a regular auto-pilot flight grid, certain flight lines had to be manually piloted to adapt to the topography and local forest structure.

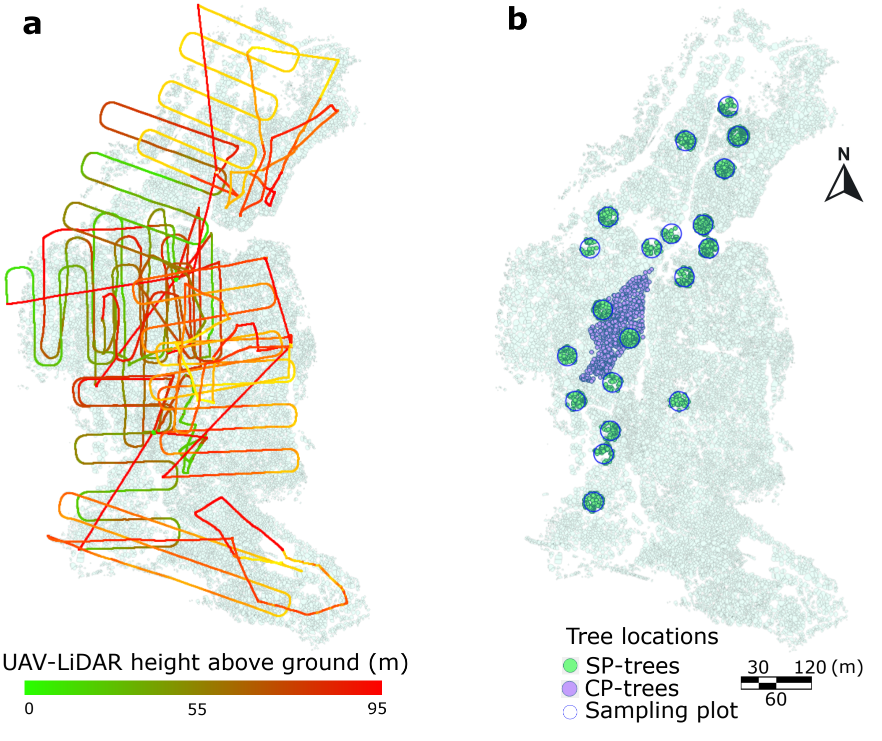

FIGURE 2 **a:** trajectories of individual flights during survey of the Unstaffed Aerial Vehicle (UAV) Light Detection and Ranging (LiDAR) sensor; color gradient indicates height above ground at take-off point. **b:** spatial distribution of field-based forest inventory. Dots represent the locations of the ground-truth labels. The sampling plot-trees (SP-trees, N = 1635 trees) are shown in green; the control plot-trees (CP-trees, N = 845 trees) are shown in purple. In both **a** and **b**, the underlying polygon dataset shows the individual tree canopies (ITC) after the canopy height model (CHM) segmentation.

The field-based measurements (shown in Figure 2, b) are taken on a yearly basis as part of a long-term ecosystem monitoring initiative—jointly organized by ICOS [63] and the Swiss Federal Institute for Forest, Snow and Landscape Research (WSL) [60]. Based on standardized methods (i.e., *Sanasilva Inventory* protocol [68]), expert field workers monitor tree crown status in terms of color and density, focusing on three groups of indicators: variations in size, density and color. The number of trees that have died since the previous survey, as well as the new ones that reached a minimum DBH of 5 cm are also recorded. As ancillary data, the following parameters are also evaluated: identified causes of defoliation, competition in the canopy, and the presence of epiphytes, mistletoe and climbing plants [69].

We treated two different datasets separately as ground-truth measurements within the same study area: control plot trees (CP-trees, 4 adjacent monitoring units) and sampling plot trees (SP-trees, 20 scattered units of 15 m radius). Several factors led us to consider both datasets separately: (i) the CP dataset is clustered and spatially continuous, while the SP dataset is spatially discontinuous and distributed along the valley. (ii) the two datasets present significant differences in morphological trait distribution (see Supporting Information, Annex IV). (iii) the variability in context metrics between the two datasets varied markedly. (iv) the field-based instrumentation and protocols used for monitoring presented minor differences between both datasets. Figure 2 (b) shows the spatial distribution of the field-based forest inventory. The CP tree position was recorded using a Leica System 1200 (GPS total station). The location and size of the sampling plots were defined according to ICOS protocols [70]. The center location of the SP plots was determined using a GPS Leica CS20 (antenna GS15) with a real-time kinematic (RTK) signal (accuracy measurements ranges from 0.03m to 0.7m). Next, the trees in the SP plots were positioned by measuring the azimuth with a field goniometer, while the horizontal distance and the inclination from the plot centers was determined using a Vertex Laser Geo meter. The accuracy of foot location of trees in the SP plots is within 0.5 m and 1.2 m. The field-based inventories used as ground-truth contain measurements taken between October 2019 and July 2021.

2.3 | Data Processing

The workflow followed in this study is presented in Figure 3. Initially, the PCD generation followed the approach described in Revenga et al. (2022) [66]. The resulting PCD scene was normalized and rasterized to obtain a canopy height model (CHM), which in turn was subject to individual tree crown segmentation [71] producing a two-dimensional polygon dataset. For the CHM segmentation, we utilized a watershed algorithm that is specifically designed for coniferous forests [71] (implemented in the LiDAR360 software [72]). The match between field-based measurements and individual tree crown (ITC) polygons was conducted based on the closest distance between the field-based GPS point measurement and the ITC polygon centroid.

In order to ensure that only the LiDAR-detected trees would be accounted for in the regression experiment, a pre-processing manual task was undertaken (marked * in Figure 3). First, understory trees that passed unnoticed to the UAV-LiDAR survey were removed. Second, we filtered clumped trees based on tree height by selecting the field-based measurement of the highest tree when two measurements were less than 1 m apart, while removing the measurement of the other tree. Third, we corrected for a crown shift effect, i.e., some high and skewed trees were affected by the presence of a smaller neighboring tree (affecting about 5% of trees) being closer to its corresponding ITC polygon centroid, thus introducing a wrong match between the field-based measurement and the LiDAR-derived metrics.

Afterwards, using the LiDAR-derived height as polygon attribute, we calculated the distance at which the spatial autocorrelation of tree height was most significant in order to define the optimal neighborhood size (as explained in Section 3.1). Once the optimal neighborhood size had been defined, we conducted the local indicators of spatial association (LISA) analysis [43, 48] and outlier analysis [73, 74] to retrieve neighborhood metrics. Finally, two separate supervised regression experiments were performed, in order to predict DBH based on LiDAR-derived metrics: one including the neighborhood metrics (context-aware regression), the other without taking those metrics into account (context-unaware regression). Finally, AGB was estimated from the predicted DBH via an allometric function (as defined in Eq. 5).

In parallel, we conducted a second task to characterize the morphometry of tree assemblages (i.e., groups of adjacent trees fulfilling a specific criterion of height similarity, as explained in Section 2.6) stemming from the ITC polygon dataset. Prior to the morphometric analysis of tree assemblages, a second pre-processing task was conducted (marked ** in Figure 3). First, ITC polygons were merged based on either local Moran's I_i [43] or SL_i [75] (see Section 2.4). These new larger polygons describe the two-dimensional projection of tree assemblages. Then, as our interest focused on the extent and shape of the tree assemblages, the inner borders of the merged polygons were disregarded. To reduce computation time, the polygon shapes were simplified by reducing the number of vertices and edges to 70 % while keeping the polygon shape.

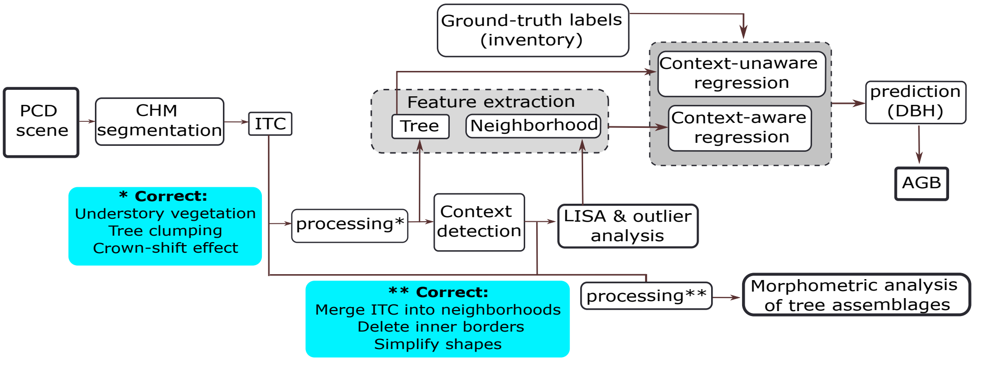

FIGURE 3 Workflow followed in this study. PCD: point cloud data, CHM: canopy height model, ITC: individual tree crown, LISA: local indicators of spatial association, DBH: diameter at breast-height, AGB: above-ground biomass. The two colored boxes describe the subtasks constituting each of the processing steps, marked * and ** in the diagram.

2.4 | Definition of Context Via Tree Neighborhood

We determined at what distance neighborhood metrics should be calculated (i.e., how many surrounding trees should be accounted as neighbors) based on local similarity of tree height. Accordingly, the selection of an appropriate neighborhood size around each individual tree (i.e., context detection) [76] was calculated through the analysis of spatial autocorrelation as function of incremental distance. Based on the global peak in the significance of spatial autocorrelation, we defined a characteristic distance within which all included trees should be considered as neighbors. All so-defined neighbor trees were accounted for to compute context-aware metrics.

The local context information was encoded as metrics derived from the individual tree heights in each neighborhood, calculated at each tree location. Specifically, the metrics computed to define tree neighborhoods were: local Moran's I [43] clustering (i.e., an estimate of local significance of similarity with respect to global variance); and (SL_i) of tree height (i.e., a weighted average of heights calculated entirely locally) [75].

2.5 | Neighborhood Information as Predictive Features

2.5.1 | Neighborhood Metrics

Local Moran's I_i is a well-established distance statistic in spatial data analysis [77], used for detecting local spatial autocorrelation and included within the family of LISA methods [48]. Like other methods [78], it relates attribute similarity with locational similarity, mapping autocorrelation across the geographic space. In the following definitions, σ is the global sample standard deviation of tree height; n and m represent the total number of instances (i.e., all trees in the forest) and the number of neighbors to each tree, respectively; y_i indicates the magnitude of interest at a particular point of interest (i.e., tree height) while the overline (i.e.,$\overline{y}$) indicates global average; $w_{i,j}$ indicates the distance weighting of each neighboring tree (here defined as inverse distance weighting); subindexes i and j indicate the tree of interest and a neighbor tree, respectively. Let $y_1, \ldots, y_n$ be the tree height values of all the n trees in the dataset. Then, the Local Moran I_i [43] is defined as

$$I_i = \frac{y_i - \overline{y}}{\sigma^2} \sum_{j \in \mathcal{N}_i, j \neq i} w_{i,j} (y_j - \overline{y}), \tag{1}$$

where $\mathcal{N}_i \subset \{1, \ldots, n\}$ is the set of indices corresponding to the nearest neighbors of tree $i \in \{1, \ldots, n\}$ in the overall set, with $\sum_{j \in \mathcal{N}_i, j \neq i} w_{i,j} = 1$ and where

$$\overline{y} = \frac{1}{n} \sum_{i=1}^{n} y_i, \tag{2}$$

and

$$\sigma = \sqrt{\frac{\sum_{i=1}^{n} (y_i - \overline{y})^2}{n-1}}, \tag{3}$$

are the global average height and the global sample standard deviation, respectively. It should be noted that insofar I_i includes global metrics (such as n, σ and $\overline{y}$), it is not entirely locally computed, but may present correlation with global features (i.e., characteristics derived from the entire dataset) [79]. The Spatial Lag (SL_i) of tree height for a tree i is a spatial smoother [80] defined as:

$$SL_i = \sum_{j \in \mathcal{N}_i, j \neq i} w_{i,j} y_j \tag{4}$$

Therefore, SL_i can be seen as a weighted average of the attributes of neighboring trees [81]. The neighborhood metrics finally chosen as context-aware predictors are the following: local Moran's Index (I_i), z-score of I_i, p-value of I_i, z-transformed value of I_i and SL_i - computed at 20 m, 30 m , 40 m and 50 m distance bands. Additionally, the mean heights of the k-nearest trees, with k $\in (5 - 75)$, were also included.

2.5.2 | Environmental Variables

We also included the topographic wetness index (TWI) [82] as environmental variable. TWI is a steady state wetness index used to evaluate topography-dependent surface hydrology processes. According to [82], TWI is defined as $\frac{a}{tan(b)}$, where *a* represents the upslope area draining through the point of interest, and *b* indicates the local slope. The parameterization considered to calculate TWI followed the suggestions of Kopecký et al. (2021) [83] for estimating soil moisture. In order to discern how much the contribution of TWI is influenced by granularity, we calculated it at a 2 m^2 resolution, and resampled to 5 and 10 m^2, via bilinear interpolation. Therefore, TWI was included at a spatial resolution of 2, 5 and 10 m^2 as separate predictors.

2.6 | Tree Assemblages: Definition and Morphometry

In order to define tree assemblages, local Moran's I_i and SL_i were both computed at the optimal distance band to obtain neighborhood metrics, i.e., based on the global peak in the significance of spatial autocorrelation as a function of distance (using ArcGIS Pro software [84]). Tree assemblages were therefore defined as geographically continuous groups of trees delineated according to either (i) variation of local Moran's I_i of tree height, or (ii) according to quantiles of SL_i of tree height. The rationale for using two different statistics to calculate tree neighborhood metrics and thus delineate different tree assemblages was that while SL_i is entirely locally calculated, local Moran's I_i includes global features (and is therefore sensitive to the statistical characteristics of the dataset as a whole), as explained in Section 2.5.1. In order to discern which of the two approaches seemed most convenient in delineating tree assemblages (the former *entirely* local; the latter only *partially* local), both were included.

Tree assemblages defined according to local Moran's I_i are geographically continuous groups of trees with significantly different heights than the global tree height average, and they also lie in a region with significantly different neighbors. Local Moran's I_i identifies regions where the clustering of either high or short trees occurs. In the standard notation [75] (i.e., *High-High* or *Low-Low*), the first term refers to the individual tree and the second to the neighborhood (e.g., a tree belonging to a *High-High* assemblage is a "significantly high tree" in a "significantly high neighborhood"). The areas not showing statistical significance (p-value $\geq$ 0.002) were labeled as *Not-Significant*. The significance test is based on random permutations (n = 499) of neighboring tree-height values at each step in the computation. Then, for every permutation, a local Moran's I_i value is calculated by randomly rearranging the tree heights of neighboring values. The result is a randomly generated reference distribution of expected local Moran's I_i that is compared against the observed local Moran's I_i (Eq. 1) [48]. In this way, tree assemblages defined according to local Moran's I_i are classified as: *High-High*, *Low-Low*, or *Not-Significant*.

Likewise, tree assemblages defined according to SL_i of tree height are geographically continuous groups of trees delimited according to the local weighted average of tree height [81], as defined above (Eq. 4). For the purpose of this study, 5 subdivisions based on quantiles were deemed convenient, rendering a classification of tree assemblages based on SL_i ranking as: *Highest*, *High*, *Mid*, *Low* and *Lowest*.

The morphometric analysis used as its objects of analysis the outer boundaries of tree assemblages, defined either by local Moran's I_i or SL_i of tree height, as defined above. Twenty basic morphometric parameters as well as 20 derived parameters were calculated for each type of tree assemblage. The 20 basic morphometric variables are simple parameters obtained by fitting elemental geometric shapes to each tree assemblage polygon (e.g., area of maximum inscribed circle), and basic positional parameters (e.g., XPOL, which is the X coordinate of the centroid of the tree assemblage polygon). The 20 derived parameters are adimensional metrics (except for concavity [85], measured in m) computed from the 20 basic morphometric variables, as explained in [86] (a full description of the 40 morphometric parameters is given in Annex I). The morphometric analysis of tree assemblages was conducted using PolyMorph-2D algorithm [86], which is a toolbox for the morphometric analysis of vector-based polygon objects, available as a plug-in for the open source JumpGIS software [87].

2.7 | Regression Models Selected

The regression experiments were designed to predict DBH, since AGB is a variable determined by the combination of DBH, height and wood density. The AGB estimates were derived from the DBH prediction outputs by means of an allometric fit (Eq. 5). Predicting DBH, instead of AGB directly was chosen as more suitable, as it avoids burdening the learning models with the statistical error contained in the allometric fit. Several feature-based regression methods were selected: namely AdaBoost [88, 89], Lasso [90] and Random Forest [91] regressors.

The AdaBoost regressor [92] is a gradient-boosting method based on stage-wise additive expansions; its effectiveness rests on the combination of weak learners (i.e., decision trees) to produce a generalized prediction hypothesis. Lasso is a linear model with *L1* prior penalty as a regularizer [93], while Random Forest is a tree-based ensamble regression method. In our case, all three feature-based methods take as input the features derived from the ITC polygon dataset resulting from the CHM segmentation.

Context-unaware regressions are defined as those in which a learning model performs DBH regression by taking as predictors only individual tree attributes derived from the ITC polygon dataset (i.e., tree height, canopy area and canopy perimeter), as it is a common approach [28]. We defined context-aware regressions as those regressions in which context-aware features are additionally introduced as input. These come in the form of either neighborhood metrics, e.g., SL_i of tree height, or as environmental variables, i.e., TWI at different spatial resolutions. Both the neighborhood metrics and environmental variables used are described in Section 2.5.1 and Section 2.5.2, respectively. For every model predicting DBH from individual tree attributes (i.e., context-unaware conditions) we implemented a context-aware counterpart.

2.8 | Training, Validation and Test

A hard validation of AGB is not possible without harvesting trees destructively, which raises obvious ethical, legal and economic issues. Thus, non-invasive methods that use RS data and allometric functions are the standard procedure for estimating AGB [18]. Here, we chose two variables to validate our predictions: (i) DBH, a key morphological trait contained in the field-based forest inventory; and (ii) tree-level AGB estimates derived via species-specific allometric and wood density functions. Specifically, the allometric model used was the one proposed by Dalponte and Coomes (2016) [94]:

$$AGB_{tree} = \alpha \cdot WD_{spruce}^{\beta} \cdot (DBH - d_0)^{\gamma} \cdot H^{\delta}, \tag{5}$$

where the wood density value (WD_{spruce}) was taken from Alpine spruce dendrometric models [95]; diameter at breast-height (*DBH*) and height (*H*) are allometric measurements, while $\alpha, \beta, \gamma, \delta$ and d_0 are species-specific fitted parameters [96]. The AGB assessment was derived from the predictions of DBH (and LiDAR-derived height) in either aware or unaware conditions. Therefore, the predicted value of DBH was input into Eq. 5, in order to obtain predictions of AGB. This allowed to compare AGB predictions to the ground-truth values of AGB, which were similarly obtained via the field-based measurements (provided by the regular tree-monitoring campaigns of ICOS [63] and

WSL [60]) and Eq. 5.

For training and validating the regression models, the instances with empty ground-truth labels were initially removed (i.e., trees with no DBH or tree height recorded). Afterwards, data stratification was done via five commonly used percentiles (i.e., 0-10, 10-25, 25-50, 50-75, 75-90, 90-100) to ensure that input data is independently drawn from an identical sample distribution (i.i.d. assumption) [97]. This assured us that most parts of the target distribution are represented, in particular the tail ends. Then, the technique used to estimate model prediction error consisted of a nested cross-validation (NCV) [98]. Following the NCV scheme, we divided the input dataset (either CP, or SP, correspondingly) into 10 inner and 10 outer folds. The inner cross-validation was used for hyperparameter optimization and feature selection, while the outer cross-validation was used to evaluate model performance (the method description is extended in Section 4.4 and further details are given in Annex III). The significance of the enhancement in context-aware predictions and effect size was assessed using Wilcoxon signed-rank test [99] and Cliff's Delta analysis [100], respectively.

3 | RESULTS

3.1 | Context Detection and Tree Assemblage

The selection of the specific distance for computing tree neighborhood metrics was calculated based on the degree of spatial autocorrelation of tree height by incremental distance, as in previous studies [101]. This resulted in a global maximum at a distance of 40 m. Figure 4 (a) shows the calculation of local Moran's index (I_i) of tree height at different distance bands. Figure 4 (b) shows the z-score of I_i obtained at each distance band, resulting from comparing the observed I_i and the expected I_i under the tree height randomness assumption (details included in the Annex II). As a sanity check, we ran context-aware regression experiments including context features retrieved at shorter (i.e., 20 m, 30 m) and larger (i.e., 50 m) distances than the optimal range (i.e., 40 m). The context features retrieved at these distances and contributing to improved predictions of DBH were also included in the final regression models.

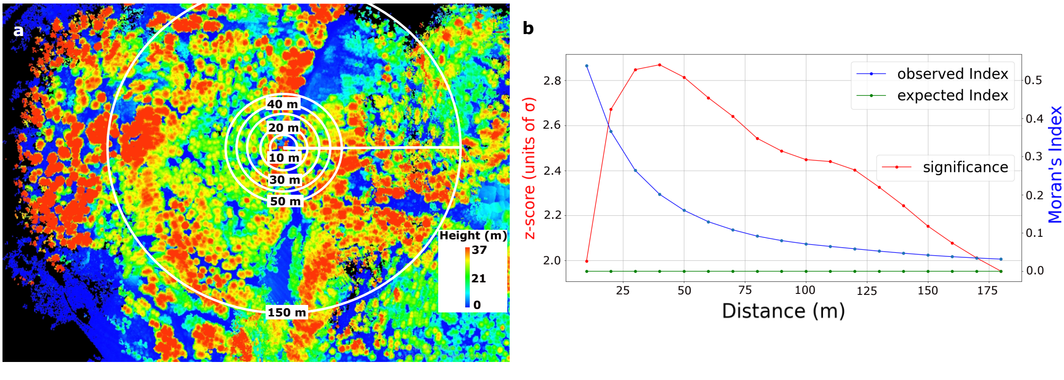

FIGURE 4 Context detection. **a:** normalized point cloud data (PCD) scene colored by tree height overlaid with a selection of the appropriate radii for defining the neighboring context. **b:** Autocorrelation of tree height as function of distance. The red line shows the number of standard deviations (σ) that an observation is away from the expected value (under the assumption of heights being randomly distributed). The blue and green lines show the actually observed local Moran's Index and the expected value under randomness assumption, respectively.

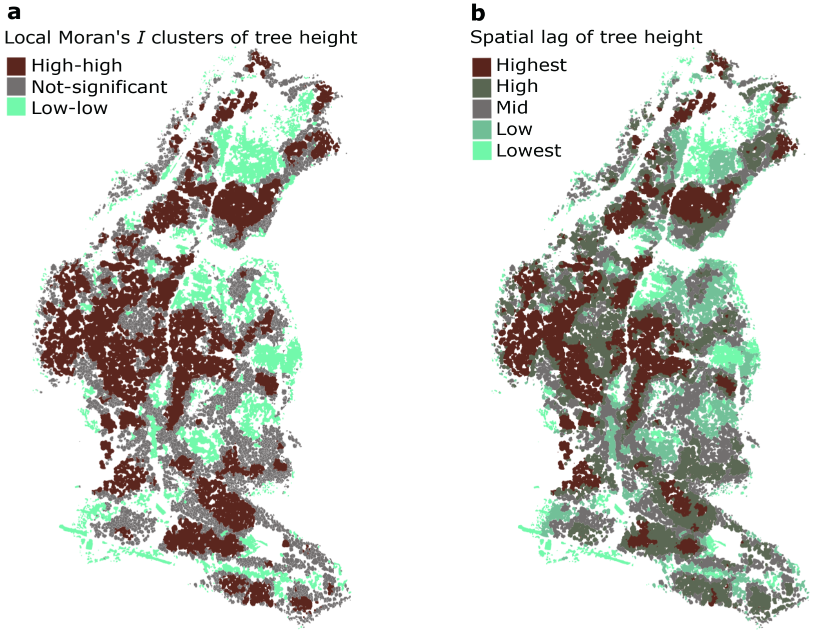

FIGURE 5 Tree assemblages defined by local similarity of tree height. **a:** delineated according to local Moran's I_i of tree height; **b:** delineated according to spatial lag of tree height.

Figure 5, a and b, show the spatial distribution of different tree assemblages defined by local Moran's I_i and by SL_i of tree height respectively. While both types of assemblages show similarities as regards extent and location, SL_i captures more local variability. This is not only due to a higher discretization (5 groups in SL_i, vs. 3 groups in local Moran's I_i), but also to the fact that SL_i is insensitive to the variance in the dataset beyond the range of its neighborhood, as explained in Section 2.5.1 (in Figure 5, both assemblage types shown in Figure 5 were derived from these two metrics, calculated at 40 m range).

Figure 6, panels a and b, show the results of the morphometry analysis of tree assemblages defined by local Moran's I_i and by SL_i respectively. The results are based on the shape of the outer contours of the resulting tree assemblages. The circular barplots show the average magnitude as bar lengths, and the standard deviation as dots. Both mean and standard deviation values are shown as min-max scaled (across assemblage types) to present all variables on the same radial axis and to ease visual comparison, i.e., for every morphometric variable, the highest value is replaced by 1, the minimum is replaced by 0, and the intermediate values are linearly interpolated between 0-1.

While not for all variables a systematic trend was found, for several basic morphometric variables a clear positive correlation between them and SL_i was observed. This is the case for polygon area, perimeter of polygon (PPOL) and radius of the minimum circumscribed circle (RMCC). Additionally, a positive correlation was found for some derived morphometric variables, namely: length-to-width ratio (LTWR) [102], circularity ratio (CIRR) [105], compactness factor (COMF) [86], dispersion measure (DISM) [105], complexity index (COMI) [86], lemniscate ratio (LEMR) [109], regularity factor (REGF) [104], and concavity (CONC) [85]. Conversely, other morphometric variables showed a decreasing trend with increasing SL_i. A negative correlation between SL_i and the following derived morphometric variables was found: Miller's circularity ratio (MCIR) [107], Horton's form factor (HFOR) [102], elongation factor (ELOF) [108], shape factor (SHAF) [104], convexity [110], solidity [111], rectangularity (RECT) [112] and roundness (ROUN) [110].

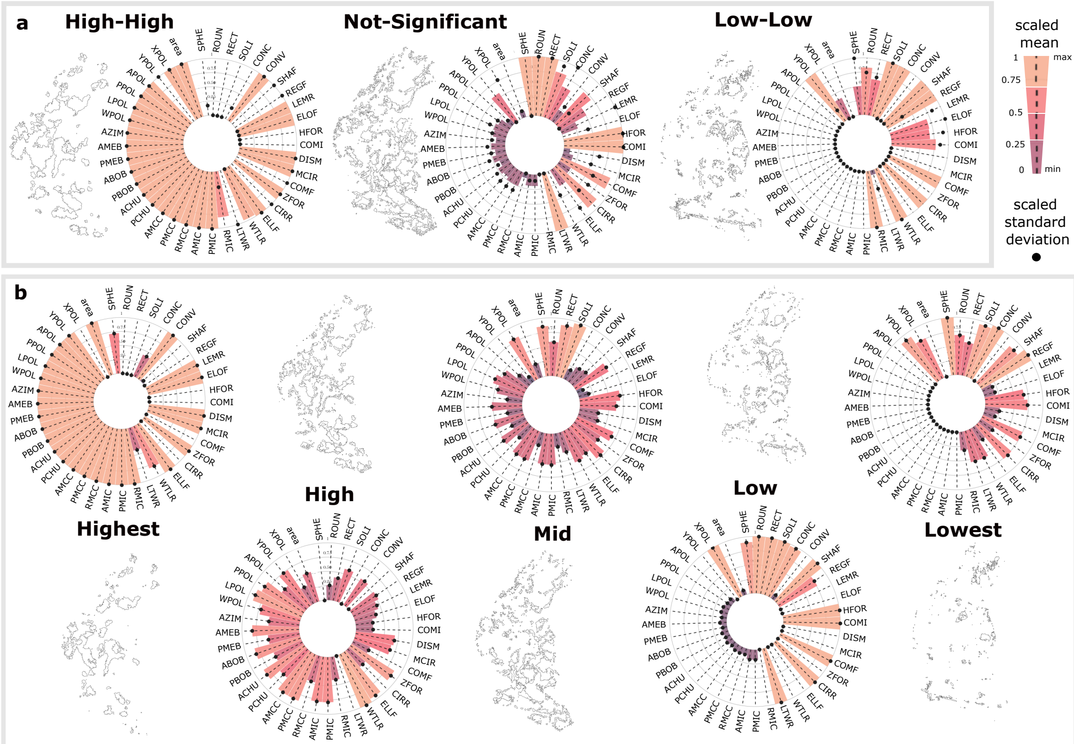

FIGURE 6 Morphometric analysis of tree assemblages grouped by **(a)** local Moran's I_i, and **(b)** by spatial lag of tree height. Bar length and color gradient represent the mean value, while black dots represent the standard deviation (SD) over all tree assemblages. Both mean and SD are scaled (min-max) to allow comparison of all metrics across assemblage types on the same axis (i.e., for every morphometric variable, the highest value of a certain assemblage type is replaced by 1, the minimum value is replaced by 0, and the intermediate values are linearly interpolated in between the range (0-1)). YPOL: northing of centroid of the tree assemblage; XPOL: easting of centroid of the assemblage; APOL: area of polygon (P); N-S: defined as $|sin(azimuth)|$, shows the alignment of the main axis of P with the North-South direction; PPOL: perimeter of P; LPOL: major axis length (L) of P; WPOL: minor axis length (W) of P; ABOB: area of the bounding box fully containing P; PBOB: perimeter the bounding box fully containing P; AMEB: area of the minimum enclosing box fully containing P; PMEB: perimeter of the minimum enclosing box fully containing P; ACHU: area of containing hull ; PCHU: perimeter of convex hull fully containing P; AMCC: area of the minimum circumscribed circle (MCC); PMCC: perimeter of MCC; RMCC: radius of MCC; AMIC: area of maximum inscribed circle (MIC); PMIC: perimeter of MIC; perimeter of MCC; RMIC: radius of MCC; LTWR: length-to-width ratio [102]; WTLR: width-to-length ratio [103]; ELLF: ellipticity factor [104]; CIRR: circularity ratio [105]; ZFOR: Zavoianu's form factor [106]; COMF: compactness factor [86]; MCIR: Miller's circularity ratio [107]; DISM: dispersion measure [105]; COMI: complexity index [86]; HFOR: Horton's form factor [102];ELOF: elongation ratio [108]; LEMR: lemniscate ratio [109]; REGF: regularity factor [104]; SHAF: shape factor [104]; CONV: convexity [110]; CONC: concavity [85]; SOLI: solidity [111]; RECT: rectangularity [112]; ROUN: roundness [110]; SPHE: sphericity [113].

The correlations between local Moran's I_i and morphometric variables followed the same trends as for SL_i. An observed difference between SL_i and local Moran's I_i was found in the heteroscedasticity of the morphometric variables calculated. In the former case, we observed that the variance of all metrics scaled with magnitude (i.e., constantly increasing variance), while in the latter an irregular trend was found (i.e., an uneven trend in the variance). We visualized these observations in the distribution of scaled mean values and scaled standard deviations in Figure 6, a and b.

3.2 | AGB Predictions: Aware vs. Unaware of Local Context

Regression experiments including context-aware features improved predictions of DBH consistently (see Tables 1 and 2), resulting in spatially resolved enhanced tree-level AGB predictions via allometry (Eq. 5). Although consistent, the degree of prediction enhancement differed between both datasets considered. Predictions in the CP-dataset observed a lower enhancement in comparison to predictions in the SP-dataset. For instance, RMSE was reduced by 9.1% (SP-dataset) vs. 4.0% (CP-dataset), and R2 increased by 3.5% (SP-dataset) vs. 3.2% (CP-dataset). This was expected, due to less variability in context in the CP-dataset.

In Figure 7, the left panel (a) shows the ground-truth labels (i.e., field based estimates of AGB), which were derived from the field measurements and a species-specific allometric fit (i.e., Eq. 5). The central panel (b) shows the spatial distribution of residuals (i.e., $\epsilon = AGB_{ground-truth} - AGB_{prediction}$) of the AdaBoost context-aware regression results. The mean values converge towards zero (i.e., $\overline{\epsilon}_{SP} = 3.8$ kg , $\overline{\epsilon}_{CP} = -3.2$ kg), while the spread of the error distribution varies between SP and CP datasets (i.e., $\sigma(\epsilon_{SP}) = 123$ kg, $\sigma(\epsilon_{CP}) = 140$ kg).

The lack of high spatial autocorrelation of errors (i.e., low clustering of errors) indicates that predictions are not geographically biased. The upper-right panel (c) displays the error distributions in both datasets. SP-errors show a unimodal distribution with a slight overestimation of DBH of -28 mm (i.e., overestimation). CP-errors present a similar overestimation bias (-25 mm) with a bimodal distribution (the second mode is located at 25 mm of underestimation). The two bottom-right panels show the error distribution of DBH predictions along the ground-truth measurements of DBH and tree height, respectively. It can be observed that, generally, smaller and thinner trees tend to be slightly overestimated (i.e., in the first two quantiles), while the largest trees (i.e., quantile 5 and highest trees) tend to underestimation.

Figure 8 presents a detailed analysis of the relative importance of all predictors considered in the context-aware DBH regression with the AdaBoost regression model. We used the permutation importance inspection technique as proposed by Altmann et al. (2010) [114]. The analysis reveals that in both SP and CP datasets, the most important context-aware predictors are the average heights of the 5, 10, and 15 nearest neighboring trees, outperforming some individual-tree metrics, such as the crown metrics.

TABLE 1 Results (on test set) of the sampling plot (SP) dataset. Predictor variables are LiDAR-derived features; target variable is diameter at breast-height (DBH, in mm). The values are presented as mean ± standard deviation of the 10 outer CV folds. One asterisk (*) marks results where the enhancement introduced by context-awareness is statistically significant with "small" size effect, while ** and *** mark "medium" and "large" size effect, respectively. The best results are shown in bold.

Regression model	R^2	RMSE (mm)	MAE (mm)	MAPE (%)
AdaBoost (unaware)	0.830 ± 0.05	58.0 ± 9.0	43.3 ± 4.4	19.1 ± 1.9
AdaBoost (aware)	**0.860 ± 0.03** ***	**52.7 ± 5.3** ***	**41.0 ± 3.1** **	**19.5 ± 1.7**
Random Forest (unaware)	0.818 ± 0.04	60.2 ± 7.3	46.8 ± 4.5	22.8 ± 5.8
Random Forest (aware)	0.838 ± 0.05 *	56.5 ± 9.2 *	41.6 ± 5.4 ***	22.4 ± 5.1
Lasso (unaware)	0.851 ± 0.02	54.6 ± 4.9	4.20 ± 3.3	19.1 ± 1.4
Lasso (aware)	0.852 ± 0.02	54.4 ± 4.9	4.17 ± 3.5	18.8 ± 1.7

TABLE 2 Results (on test set) of the control plot (CP) dataset. The predictive variables are LiDAR-derived features; the target variable is diameter at breast-height (DBH, in mm). The values are presented as mean ± standard deviation of the 10 outer CV folds. One asterisk (*) marks results where the enhancement introduced by context-awareness is statistically significant with "small" size effect. The best results are shown in bold.

Regression model	R^2	RMSE (mm)	MAE (mm)	MAPE (%)
AdaBoost (unaware)	0.713 ± 0.07	54.7 ± 5.98	43.0 ± 5.26	15.5 ± 2.4
AdaBoost (aware)	0.737 ± 0.05 *	52.9 ± 5.28 *	42.2 ± 4.43 *	15.7 ± 3.1
Random Forest (unaware)	0.688 ± 0.07	57.0 ± 5.9	43.8± 5.1	15.7 ± 3.1
Random Forest (aware)	0.705 ± 0.04	55.6 ± 5.3	41.3 ± 5.5 *	15.9 ± 4.3
Lasso (unaware)	0.741 ± 0.09	51.3 ± 6.6	39.1 ± 5.2	13.6 ± 1.6
Lasso (aware)	**0.750 ± 0.08**	**50.4 ± 5.9**	**38.6 ± 4.1**	**13.6 ± 1.1**

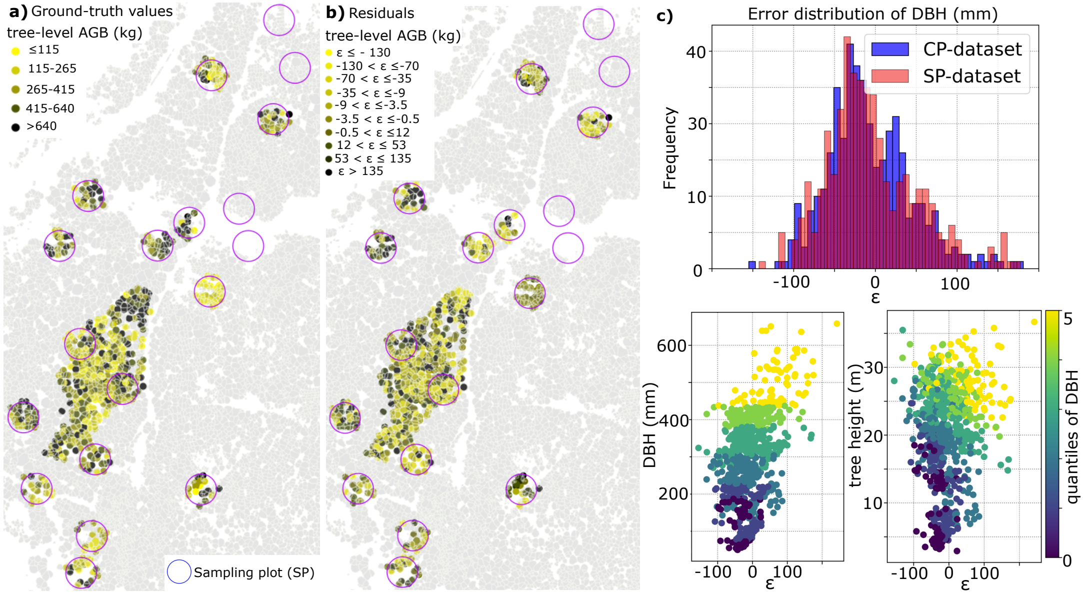

FIGURE 7 **a**: spatial distribution of tree-level above-ground biomass (AGB) according to ground-truth measurements (provided by the tree-monitoring campaigns of ICOS [63] and WSL [60]) and Eq. 5, grouped by quantiles. **b:** spatial distribution of residuals ($\epsilon = AGB_{ground-truth} - AGB_{prediction}$) of AGB predictions with AdaBoost context-aware regression, grouped by quantiles. Negative values indicate overestimation. The empty SP-plots correspond to areas where the quality of the UAV-LiDAR data collection was compromised. **c**: error distributions of diameter at breast-height (DBH) in sampling plot (SP) and control plot (CP) datasets. The two bottom-right panels show the error distribution of DBH (in x-axis) vs. field-measurements of DBH and tree height.

4 | DISCUSSION

4.1 | Enhancement of Tree-Level AGB Prediction

This study presents a method of enhancing tree-level AGB estimates in forests using UAV-LiDAR surveying and context-aware ML regression methods. The results consistently showed that context-aware regressions outperformed context-unaware regressions across models. This finding indicates that gradients in morphological tree traits across the ecosystem may be a proxy for unveiled environmental and biotic factors (e.g., windstorm disturbance, nutrient and soil moisture abundance, light harvesting competition [44, 45]) that influence tree growth, which can be leveraged to enhance predictions of AGB.

The accuracy enhancement gained from including context-aware features in the regression experiments varied between the two datasets considered (i.e., SP-trees and CP-trees). Context-aware regressions of DBH in SP-trees experienced greater enhancement than CP-trees. This is consistent with the fact that the CP-dataset contains less variability of context, since it is a clustered and more homogeneous dataset, while the SP-dataset includes more variability in context-aware features. The investigated mono-specific forest presents a heterogeneous landscape, where the distribution of tree heights varies in space. Hence, the UAV-LiDAR survey gives rise to a non-stationary tree dataset [76], showing both smooth gradients and sharp changes in height values, a non-trivial question in tree-phenotyping and species mapping [50]. As SP-trees are grouped in scattered plots across the forest, their spatial

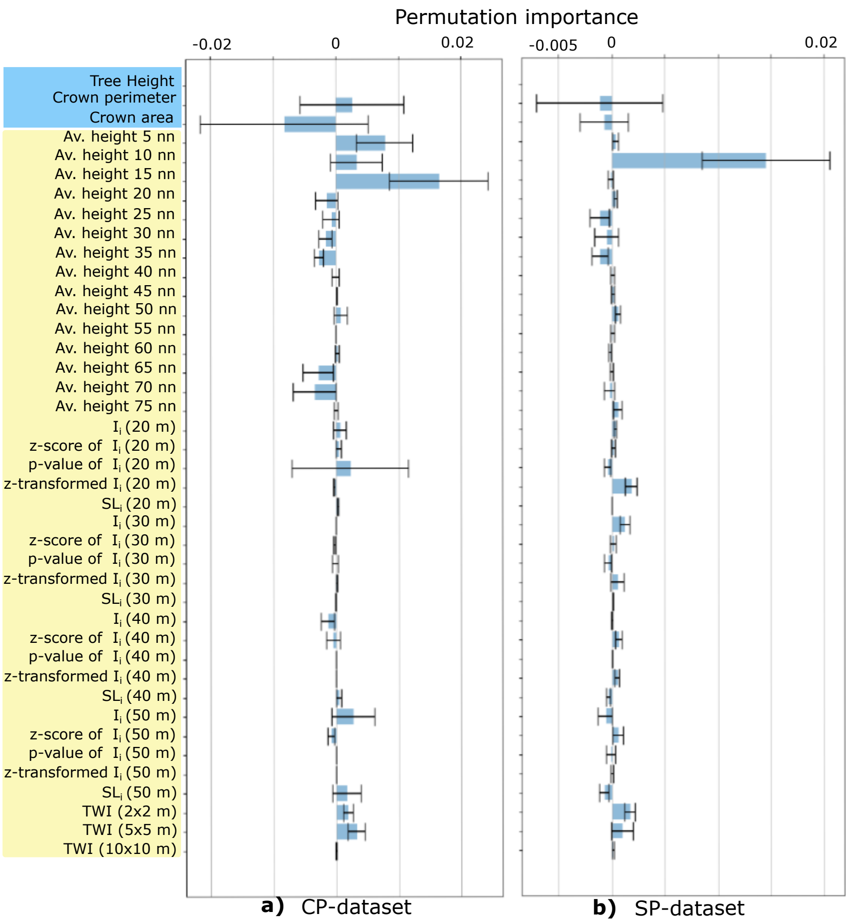

FIGURE 8 Inspection of predictors' importance via the permutation method [114] in AdaBoost regression experiment in context-aware conditions. The left panel **(a)** shows results in the control plot (CP)-dataset, and the right panel **(b)** shows results in the sampling plot (SP)-dataset. Bar length and error bar show the mean and standard deviation of a predictor's importance, respectively. A negative mean value indicates that a predictor is less useful than when being randomly shuffled, so it lowers the model's predicting performance. Predictors highlighted in light blue are individual tree traits; predictors highlighted in light yellow are context-based (i.e., either neighborhood metrics or environmental variables). In both datasets, it can be noted how the average heights of the nearest neighbors (nn) stand out as the strongest context-based predictors. In both plots (**a** and **b**), individual tree height has been removed to ease visual comparison of the remaining predictors.

distribution spans hundreds of meters, making them subject to a more diverse context than the very local CP-dataset.

4.2 | The Role of Neighboring Context in AGB Prediction Performance

All regression models achieved enhanced predictions when contextual information was considered. Thereby, the degree of local similarity of tree height (i.e., SL_i, local Moran's I_i) was most important and, to a lesser extent, environmental variables (i.e., TWI).

Conversely, including features informing about neighbor dissimilarity, such as local outliers detected using Local Outlier Factor [73] and Isolation Forest [74] algorithms did not result in enhanced predictions. We hypothesize that metrics containing information about the degree of local similarity may reveal the combined effect of ecological processes that are specific to the immediate neighboring context. Conversely, metrics containing information of the dissimilarities of the individual trees do not help to uncover such processes, but remain useful in detecting outstanding trees (i.e., local outliers).

Context-based features at closer distances generally showed larger predictive power but also larger variance (as less neighboring trees are computed), therefore producing a strong and fluctuating signal, that in some cases was challenging for the ML model to incorporate in the learning process. For instance, the p-value of Local Moran's I_i at a 20 m range in the CP-dataset has an average positive effect but is not a stable predictor (Figure 8, a). This can be observed in the general trend of larger standard deviations in the permutation importance of predictors retrieved at short ranges than at greater distances (Figure 8). After the peak in the spatial autocorrelation of tree height (i.e., at larger distance bands than 40 m), the significance of clustering of tree height values declined, presenting another shoulder at a distance of 110 m (Figure 4, b). As the neighborhood size increased beyond the 40-meter distance range, the predictive power of the metrics derived from the neighboring trees (i.e., the influence of local context) progressively smoothened down [80].

In accordance with competition-based studies [32, 33, 34], we observe that the strongest context-based predictors are those retrieved from the immediate neighboring trees in both datasets, i.e., the average height of 5, 10 and 15 nearest neighbors (Figure 8). This observation indicates that individual tree structural traits are primarily mediated by competition mechanisms. However, our method additionally allows to compare the relative importance of competition-derived metrics and other context-based metrics operating at larger scales. For instance, in Figure 8 (a) it is shown that local Moran's I_i retrieved at a 50 m range is comparable in importance to the average height of the closest 10 neighboring trees.

A general difference observed between the CP and the SP dataset is that the predictors' importances in the CP-dataset fluctuate more (i.e., larger standard deviations). Further, in the SP-dataset, predictors rarely become negative and if they do, it is to a lesser extent. Given its broader spatial distribution and greater contextual variability, we contend that the SP-dataset can be regarded as a more representative sample of the entire forest population compared to the clustered CP-dataset. Consequently, the finding that context-based features demonstrate greater stability within the SP-dataset is noteworthy.

In relation to the environmental metrics used, TWI exhibited a greater impact on improved predictive performance at finer spatial resolutions in both datasets (Figure 8), whereas its contribution decreased at coarser resolutions (e.g., it did not significantly contribute as a predictor at 10 m resolution). This observation indicates that the spatial resolution at which TWI is most informative of individual tree traits, is similar to the usual tree crown size (i.e., 2-5 m resolution), while at larger scales its contribution as predictor becomes negligible.

The morphometric analysis (Figure 6, a and b) provided 40 additional features that were evaluated as potential predictors of DBH. However, including morphometric variables calculated from the tree assemblages in the regression experiments—either defined by SL_i or by local Moran's I_i—did not result in improved predictions of DBH. As shown in Figure 5, the shape of tree assemblages shows sensitivity to the method used. The shapes of tree assemblages indicated a trend of convergence assembly patterns at the group level [115], as discussed in Section 4.3. Nevertheless, the group morphometry did not prove useful to improve predictions of DBH.

Including context to enhance estimates of structural traits at the individual tree level has previously been proposed in seminal works [36] and been adopted subsequently for various applications in forest research [35, 37]. Lo and Lin (2012) [34] proposed a competition-specific index to capture the effect of the competing pressure of immediate neighbors. More recent research conducted in this area [32, 33] has motivated the further development of competition-aware approaches to improve the prediction accuracy of individual tree traits, using overstory tree traits as predictors, such as tree height and crown metrics, which enables the potential transferability of these methods to a RS framework.

In forest biomass research, a commonly recognized approach is calibrating regression models with plot-level metrics for predicting tree-level structural traits (e.g., parameters accounting for plot-level random effects in NLME methods). However, such approaches do not question the influence of the artificially-delineated plot size on prediction enhancement, even if it is observed that accuracy increases with plot width and number of tree neighbors [29, 31]. Furthermore, how diverse context-based attributes retrieved at different distance ranges affect tree-level predictions had not been investigated before. In this regard, our results show that the variability and extent of context determines its beneficial leverage for prediction of tree-level structural traits.

Our study continues this line of work and sheds light on how the local spatial context can be defined and leveraged in tree-level structural trait predictions (i.e., DBH), making a case for AGB estimates. The analysis shows that there is an optimal range to computing neighborhood metrics. In the case of the monoculture forest studied here, this corresponded to a 40 m range distance, based on the spatial autocorrelation of tree heights. Further, we found that the predictive power of context-based metrics is sensitive to context extent (i.e., the distance at which such metrics are calculated). This observation indicates that considering context based on plot-level metrics retrieved from artificially bounded units (plot-level metrics, as in [29, 30, 31]) may be seen as a suboptimal approach [116]. Likewise, in the light of this observation, and in line with recent studies [117], determining the significant contextual extent of individual functional traits based on fixed pixel-size [118] appears to be a subpar technique. Therefore, future forest research would probably benefit from including context-awareness determined by spatial association of tree traits, bearing in mind that context-detection is trait-dependent and may vary depending on dataset source (e.g., spatial autocorrelation as a function of distance is sensitive to CHM segmentation quality) and method applied (e.g., delineation of tree assemblages varied slightly between local Moran's I_i, and SL_i, as we show in Figure 5, a and b). The motivation for our study has been to introduce more quantifiable terms to ecological reasoning and to propose a standardized method of incorporating context-awareness into AGB research. The method proposed is conceived for a RS framework. Since we do not make use of external data sources but, on the contrary, every predictor is native to the UAV-LiDAR dataset, it is readily transferable.

Lastly, we note that RS studies usually define the optimal scale of analysis as a trade-off between the observational extent (i.e., area surveyed) and the unit resolution (i.e., pixel size) [117]. Also, in ecological research, it is common to subsample datasets using natural subregions based on ancillary ecological criteria (i.e., ecoregions, conservation status) [4]. Conversely, here we defined the range of influence of context-based metrics (i.e., the boundaries of tree neighborhoods) using a dataset-native approach, based entirely on the spatial association of individual tree traits. This permitted us to determine the context of influence unhampered by the RS technique and not using external data sources. In computer vision studies that investigate contextual learning, image analyses typically do not assume a specific optimal scale [119, 120], such as in geographic analysis [121]. In this study, local context was defined based on the spatial association of a real physical attribute of the target objects (i.e., tree height), and not defined by an artificially bounded unit (e.g., pixel size [118] or plot size) so that the resulting distance (i.e., 40 m) could be considered informative of the forest ecosystem.

4.3 | Tree Assemblages

The quantitative comparison of morphometric variables between tree assemblages (Figure 6) permitted to examine whether trees—grouped by local association of an individual trait—persistently show different shapes at the group level, shedding light on the relationship between context-based traits and individual tree traits. Remarkably, it was observed that tree assemblages delineated according to the weighted average of individual tree heights (i.e., SL_i) presented positive correlations with two-dimentional morphometric features at the group level.

For instance, assemblages with higher trees (i.e., labeled as *Highest* according to SL_i, or *High-High* according to local Moran's I_i) are consistently rounder, larger and more regular in shape. As visualized in Figure 6, SL_i correlates positively with shape regularity [104], two-dimensional concavity [85], length-to-width ratio [102] and size, indicating a consistent trait-convergence assembly pattern [115]. Higher trees seem to converge in most sheltered areas (i.e., thalwegs and local sub-basins) so that tree assemblages with highest SL_i tend to adopt the morphological features of the drainage network's shape (see Figure 9, in Annex I). Interpretation of this observation would go beyond the scope of this study. However, it may indicate that both the shape and location of tree assemblages of different heights are conditioned by underlying environmental and biotic driving mechanisms.

In the monoculture forest studied here, tree height clustering occurs (Figure 5, a), while spatial gradients of averaged tree height present preferential shapes and directions (Figure 5, b). These observations indicate that there is tree-height convergence and a tendency toward optimal phenotype expression (i.e., maximum growth performance) around the runoff drainage network (Figure 9, c, in Annex I). Higher trees are found in sheltered regions and concave channels—which generally benefit from more frequent runoff events and deeper soils [46, 47]. This may indicate that favorable environmental conditions (e.g., deeper soil, lower soil moisture-recession rates, greater availability of soil nutrients due to leaching) allow individuals to reach their optimal phenotype. Conversely, a lower SL_i of tree height in more exposed terrain (e.g., ridges, hilltops) indicates that environmental filtering (e.g., windstorm disturbance) or a reduced competition in light harvesting could play a significant role in determining the location of low SL_i tree assemblages (Figure 9, a, in Annex I). Thus, the relatively reduced tree height in exposed areas could indicate a passive response of tree height to harsher environmental conditions [49], an active response to higher light availability [44] or a limitation to tree growth caused by other local factors, such as lower soil depth or nutrients availability [1, 47]. Nevertheless, this study cannot provide an interpretation of such observations, as shifts in the variance of functional traits across environmental gradients (i.e., spatial patterns of trait similarity) do not bring strong evidence of either biotic or environmental filtering on their own [122].

4.4 | Methods Applied

The regression methods used (i.e., AdaBoost, Lasso and Random Forest regressors) are well-known methods that take as input features extracted from the polygon dataset obtained after CHM segmentation, abstracted from their spatial location (see Figure 3).

The NCV technique [98], used for model optimization and evaluation, follows the updated, most established recommendations to achieve an unbiased estimate of the generalization error, while making optimal use of the limited available data. The results in the inner folds report on training performance, as they are used for model optimization, while the mean performance on the outer folds is the one used for model evaluation. As a modification developed from standard cross-validation [123], NCV improves estimates of prediction accuracy and confidence intervals by accounting for the correlation between error estimates in different folds, an inconvenient phenomenon affecting standard cross-validation that may render error estimates overly optimistic (further details of how the NCV algorithm is implemented are given in Annex III).

The inspection technique used to evaluate predictors' influence on the DBH regression results was the permutation importance method [114]. The feature-elimination procedure consisted of eliminating progressively those predictors that presented a negative mean importance, as they were considered harmful to the model's performance.

In order to evaluate the statistical significance of the enhancement introduced by context-awareness, we used the Wilcoxon signed-rank test [99], while for the assessment of effect size we used the Cliff's Delta analysis [100]. These two tests were conducted in the same 10 outer folds of the NCV routine (i.e., test data) in aware and unaware conditions, so that results were compared using the exact same test data folds.

5 | CONCLUSIONS

The model performance consistently showed improvements to AGB prediction when context-aware features were included as predictors. This phenomenon was observed across regression models. Features that provide information about the tree neighborhood (e.g., SL_i of tree height, average height of k-nearest trees) contain useful information to improve predictions of different individual tree traits (e.g., DBH, AGB). This finding suggests that the information retrieved from the local context serves as a proxy for underlying mechanisms that exert influence on the variable of interest, i.e., tree heights adapt locally as a result of environmental and biotic processes [1, 46, 47].

Utilizing the spatial association of structural tree traits, e.g., tree height, to define the local context range is a more effective approach compared to methods that rely solely on plot-level data from artificially delineated units, such as the monitoring plot size [29, 30, 33]. This is because contextual features may contribute to enhanced AGB predictions at larger scales beyond the plot level. Moreover, as the method proposed uses metrics entirely native to the UAV-LiDAR dataset, it does not rely on tailored process-specific indices (e.g., competition metrics) [32, 33, 34] or ancillary data sources (e.g., biomes, conservation status, ecoregions) [4], making this approach more transferable to other regions or scales.

A promising continuation within the scope of this research is to investigate the relative importance of different context-based metrics in enhancing tree-level AGB predictions. This pathway may yield valuable insights into the predictive power of various biotic and abiotic environmental factors as explanatory variables. Furthermore, since individual adaptive responses can vary among tree populations [124], evaluating how diverging tree-height adaptations to the local conditions can be linked to tree populations and genotypes with UAV-based methods seems a valuable endeavor to pursue. In this line, recent work demonstrated that linking tree phenotyping to inheritable traits using UAV-based methods is possible with relative accuracy [125, 126, 127].

Regarding UAV-LiDAR data acquisition, we recommend establishing protocolized procedures for assessing PCD quality, in line with recent suggestions [18]. Also, standardized methods for structural tree-trait data acquisition have been proposed [19, 128]. However, as data collection surveys are commonly challenged by environmental conditions and conducted by different field experts and protocols, the need to deal with noisy and disparate datasets is likely to persist. Therefore, in order to successfully integrate ML models into real analysis pipelines in bio-geography, it will be necessary to devise methods that are able to perform in the presence of label noise [129] and dataset shift effects [97], as these, unlike benchmark datasets, are ubiquitous in real-world AGB applications.

Finally, we recommend adopting a context-aware approach in the growing number of forest AGB mapping projects [9, 11, 130]. Likewise, we recommend using metrics entirely locally computed (e.g., SL_i) to detect local patterns and leverage their use, as suggested by Westerholt et al. (2018) [79]. In this way, the metric is sensitive to neighboring differences while remaining totally independent from spatial structures beyond the border of the neighborhood (i.e., the dataset as a whole).

Acknowledgements

Helpful discussions with Thomas Friborg, Daniel Kükenbrink and Moritz Bruggisser are gratefully acknowledged. Likewise, we acknowledge the contribution of the field workers, who are responsible for collecting the forest inventory data on a regular basis, used here as ground-truth. This project received funding support from the Talent Program Horizon 2020/Marie Skłodowska-Curie Actions and the DeepCrop project (UCPH Strategic plan 2023 Data + Pool). MG also acknowledges funding by Swiss National Science Foundation project ICOS-CH Phase 3 (20F120_1982287).

Supporting Information

| Annex I: Location and Morphometry of Tree Assemblages

The spatial distribution of SL_i presents directional anisotropy, occupying preferential areas which seem to match sheltered sectors of the forest, such as concave thalwegs. Figure 9 highlights two neighboring areas with contrasting values of SL_i, indicating that surface hydrology processes and terrain exposure (i.e., terrain convexity) condition tree growth at the group level.

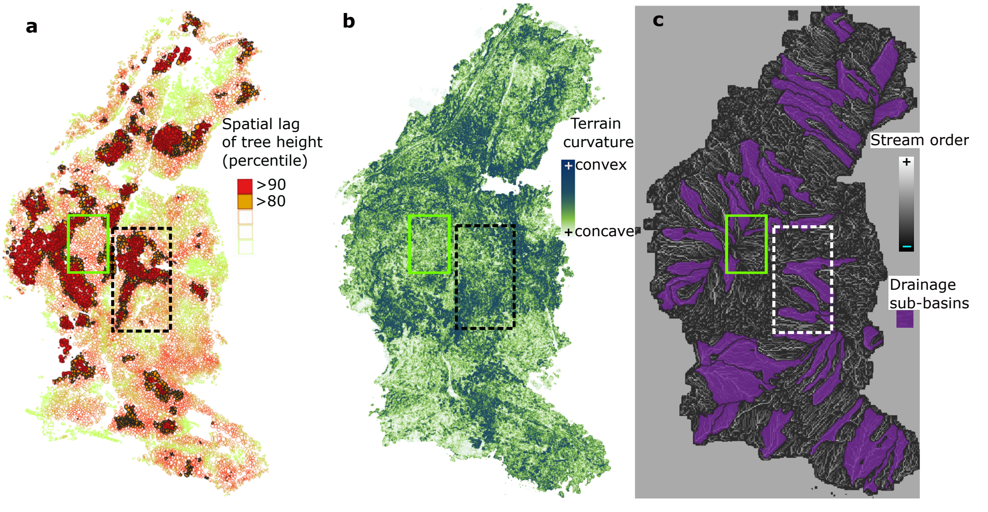

FIGURE 9 **a**: Spatial lag of tree height derived from the individual tree crown (ITC) polygon dataset. **b**: map of terrain curvature derived from point cloud data (PCD) ground-returns. **c**: Hydrological network (Strahler's stream order [131, 132]). In all three panels, the dashed box indicates an area favored by surface hydrological conditions, hosting an assemblage of trees in the >90 % percentile of spatial lag of tree height. The solid green box indicates an area at a hilltop, unfavored by surface hydrological processes, more exposed to windstorm disturbance, and hosting an assemblage of trees in the < 60% percentile of spatial lag of tree height.

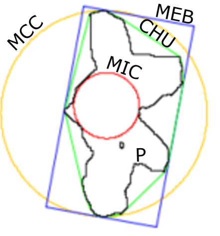

FIGURE 10 Calculation of elementary geometries fitted to an exemplary tree assemblage. P: polygon of tree assemblage (black line). MCC: minimum circumscribed cirle (in green). MIC: maximum inscribed circle (in red). CHU: convex hull (in yellow). MEB: minimum enclosing box containing P (in blue).

The morphometric analysis was conducted by taking into account the outer borders of tree assemblages defined either by SL_i, or by local Moran's I_i (delineated as explained in Section 2.6; results shownin Figure 5). The 20 basic morphometric variables (Table 3) result from fitting elementary geometries to the tree assemblage polygon. The 20 derived variables are adimensional parameters (except for concavity, measured in m) obtained by combining the basic parameters.

TABLE 3 Twenty basic morphometric variables derived from the tree assemblage polygon dataset (as described in [86]). P: tree assemblage polygon.

Basic parameters	Description	units
XPOL	Easting of P centroid	m
YPOL	Northing of P centroid	m
APOL	Area of P	m^2
PPOL	Perimeter of P	m
LPOL	Major axis' length of P	m
WPOL	Minor axis' length of P	m
N-S	North-South alignment of P, defined as $\lvert sin(azimuth) \rvert$ of major axis	$\varnothing$
ABOB	Area of the bounding box fully containing P	m^2
PBOB	Perimeter of the bounding box fully containing P	m
AMEB	Area of minimum enclosing box	m^2
PMEB	Perimeter of minimum enclosing box	m
ACHU	Area of the convex hull fully containing P	m^2
PCHU	Perimeter of the convex hull fully containing P	m
AMCC	Area of the minimum circumscribed circle enclosing P	m^2
PMCC	Perimeter of the minimum circumscribed circle enclosing P	m
RMCC	Radius of the minimum circumscribed circle enclosing P	m
AMIC	Area of the maximum inscribed circle enclosing P	m^2
PMIC	Perimeter of the maximum inscribed circle enclosing P	m
RMIC	Radius of the maximum inscribed circle enclosing P	m

TABLE 4 20 derived morphometric variables derived from the tree assemblage polygon dataset (as described in [86]). P: tree assemblage polygon. A: area of P. L: length of major axis of P. W: width of minor axis of P (i.e., width). ACHU: area of convex hull fully containing P. RMCC: radius of minimum circumscribed circle. PCHU: perimeter of convex hull fully containing P. AMEB: area of minimum enclosing box.

Derived parameters	Name	Definition	Source
LTWR	Length-to-width ratio	L/W	[102]
WTLR	Width-to-Length ratio	W/L	[103]
ELLF	Ellipticity Factor	$\lvert L-W\rvert/(L+W)$	[104]
CIRR	Circularity Ratio	P^2/A	[105]
ZFOR	Zăvoianu's Form Factor	$(16A)/P^2$	[106]
COMF	Compactness Factor	$P/(4\pi A)^{0.5}$	[86]
MCIR	Miller's Circularity Ratio	$(4\pi A)/P^2$	[107]
DISM	Dispersion Measure	$1-[(4\pi A)^{0.5}/P]$	[105]
COMI	Complexity Index	$1-[(4\pi A)/P^2]$	[86]
HFOR	Horton's Form Factor	A/L^2	[102]
ELOF	Elongation Factor	$(4A/\pi)^{0.5}/L$	[108]
LEMR	Lemniscate Ratio	$(\pi L^2)/4A$	[109]
REGF	Regularity Factor	$(\pi LW)/4A$	[104]
SHAF	Shape Factor	$[(4\pi A)/P^2]\times(L/W)$	[104]
CONV	Convexity	$PCHU/P$	[110]
CONC	Concavity	$ACHU-A$	[85]
SOLI	Solidity	$A/ACHU$	[111]
RECT	Rectangularity	$A/AMEB$	[112]
ROUN	Roundness	$(4\pi A)/(PCHU)^2$	[110]
SPHE	Sphericity	$(4A/\pi)^{0.5}/(2\times RMCC)$	[113]

Annex II: Context Detection

The distance range selected around each tree to compute neighborhood metrics (i.e., context detection), was conducted based on the peak of significance (determined using the standard z-score) of local spatial autocorrelation (using Local Moran's I_i) as function of increasing distance, in steps of 10 m (as explained in Section 3.1).

Local Moran's I_i is a spatial statistic that relates attribute similarity to locational similarity, mapping the autocorrelation of individual tree heights across the geographical space, as defined above (Eq. 1, Section 2.5.1). The expression below (Eq. 6) defines the z-score, which is used to measure the significance of tree-height clustering. Z-scores shows the significance of the clustering by subtracting the observed I_i values from the expectation (i.e., $E[I_i]$), and normalizing over the standard deviation of I_i. This produces a distance metric in units of standard deviations. $E[I_i]$ is the expected value of local Moran's I_i under the null hypothesis of no spatial autocorrelation.

$$z_{score} = \frac{I_i - E[I_i]}{\sqrt{V[I_i]}}, \tag{6}$$

Neighborhood size was determined according to the significance of spatial autocorrelation (defined as local Moran's I_i) as function of distance, via the standard z-score. Z-score measures the distance of a measured value from the expectation in units of standard deviation, under the assumption of randomly distributed values.

and the expected value of Moran's *I* under the null hypothesis of no spatial autocorrelation is:

$$E[I_i] = -\frac{\sum_{j=1}^{m} w_{i,j}}{m-1} = -\frac{1}{m-1}, \tag{7}$$

where *m* equals the total number of trees in the neighborhood. At large sample sizes (i.e., for increasing values of *m*), the expected value approaches zero. The spatial weights allocated to each neighboring tree *j* are standardized [81], such that for each tree *i*, $\sum_j w_{i,j} = 1$. The variance of local Moran's I_i is defined as the expectation of the square of I_i, minus the square of the expectations of I_i:

$$V[I_i] = E[I^2] - E[I_i]^2, \tag{8}$$

Annex III: Training, Validation and Test

Nested cross-validation (NCV) [98] is an evaluation method for determining the accuracy of point estimates and confidence intervals for prediction errors. How NCV is implemented is shown in Figure 11. The entire algorithmic routine of NCV is presented immediately below, using pseudocode. The input data (i.e., *X*,*Y*) corresponds to the set of predictors (i.e., *X*), and the target variable DBH (i.e., *Y*), respectively.

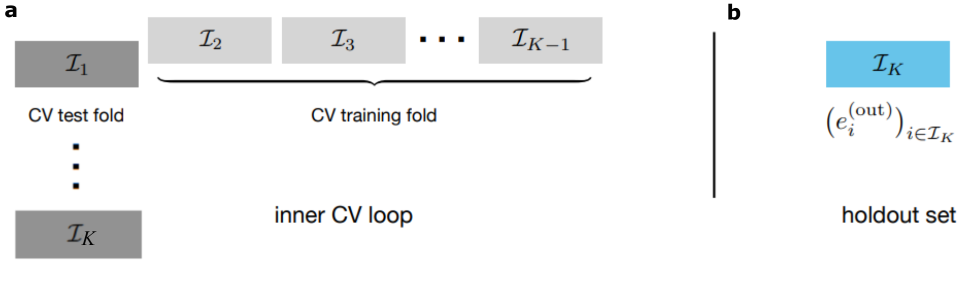

FIGURE 11 Visualization of 10-fold nested cross-validation (CV). **a**: at each of the *K* steps ($K = 10$), we perform standard cross-validation for model training (light grey folds), holding one of the folds out of the inner CV loop (dark grey fold). **b**: the fresh holdout folds (in blue) are never used for hyperparameter optimization or feature selection (figure adapted from Bates et al., 2021 [98]).

Algorithm 1: Nested cross-validation

```
Input: data (X, Y), fitting algorithm A, loss function l, number of folds K, number of repetitions R
procedure Nested cross-validation (X,Y)                    // ▷ primary algorithm;
    es ← []                                    // ▷ initialize empty vectors;
    a_list ← []                                // ▷ (a) terms;
    b_list ← []                                // ▷ (b) terms;
    for r ∈ {1, ..., R} do
        Randomly assign points to folds I_1, ..., I_K;
        for k ∈ {1, ..., K} do
                                               // ▷ outer CV loop ;
            e^(in) ← inner cross-validation(X, Y, {I_1, ..., I_K} \ I_k)     // ▷ inner CV loop ;
            θ̂ ← A((X_i, Y_i)_{i∈I\I_k}) ;
            e^(out) ← (l(f̂(X_i, θ̂), Y_i))_{i∈I_k} ;
            b_list ← append(a_list, (mean(e^(in)) − mean(e^(out)))^2) ;
            b_list ← append(b_list, var(e^(out))/|I_k|) ;
            es ← append(es, e^(in))
        MSE^ ← mean(a_list) − mean(b_list) ;
        Err^^(NCV) ← mean(es) ;
        return:(Err^^(NCV), MSE^)     // ▷ prediction error estimate and MSE estimate ;
procedure Inner cross-validation (X, Y, {I_1, ..., I_{K−1}} )   // ▷ inner cross-validation subroutine ;
    e^(in) ← [] ;
    for k ∈ {1, ..., K − 1} do
        θ̂ ← A((X_i, Y_i)_{i∈I_j∪...∪I_{K−1\k}}) ;
        e^(temp) ← (l(f̂(X_i, θ̂)), Y_i))_{i∈I_k} ;
        e^(in) ← append(e^(in), e^(temp))
    return: e^(in) ;
Output: Nested cross-validation (X,Y)
```

Annex IV: Distribution Shift Between CP-trees and SP-trees

The joint distributions of (DBH, height) in both CP and SP datasets show a shift between the two [97]. For instance, the kernel probability distribution of heights shows that the SP-dataset contains a higher amount of short trees (i.e., heights $\in (3, \ldots, 8)$ m), that cover a wide range of DBH values. Also, the range of DBH is broader in the SP-dataset compared to the CP-dataset, and the instances do not exhibit an accumulation in the center as evident as the one observed in the CP-dataset.

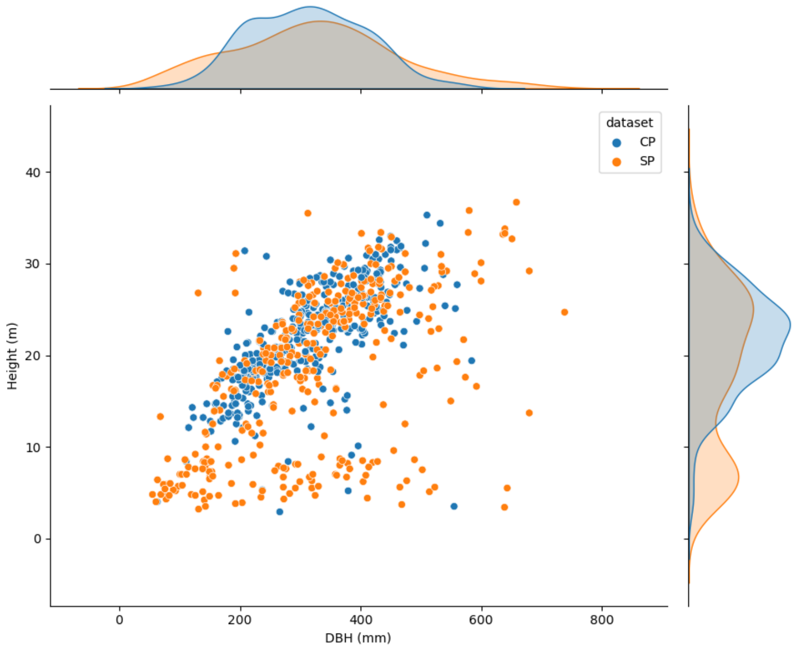

FIGURE 12 Joint distributions of diameter at breast-height (DBH) and tree height from field-based inventory data. It should be noted that the two datasets are differently distributed—i.e., there is a dataset shift [97] between sampling plots (SP) and control plots (CP) datasets.

references

[1] Fatichi S, Pappas C, Zscheischler J, Leuzinger S. Modelling carbon sources and sinks in terrestrial vegetation. New Phytologist 2019;221(2):652–668.

[2] Pörtner HO, Roberts DC, Adams H, Adler C, Aldunce P, Ali E, et al. Climate change 2022: Impacts, adaptation and vulnerability. IPCC Geneva, Switzerland:; 2022.

[3] Friedlingstein P, Jones MW, O'sullivan M, Andrew RM, Hauck J, Peters GP, et al. Global carbon budget 2019. Earth System Science Data 2019;11(4):1783–1838.

[4] Wang CJ, Zhang ZX, Wan JZ. Vulnerability of global forest ecoregions to future climate change. Global Ecology and Conservation 2019;20:e00760.

[5] Melo J, Baker T, Nemitz D, Quegan S, Ziv G. Satellite-based global maps are rarely used in forest reference levels submitted to the UNFCCC. Environmental Research Letters 2023;18(3):034021.

[6] Réjou-Méchain M, Barbier N, Couteron P, Ploton P, Vincent G, Herold M, et al. Upscaling forest biomass from field to satellite measurements: sources of errors and ways to reduce them. Surveys in Geophysics 2019;40(4):881–911.

[7] Duncanson L, Armston J, Disney M, Avitabile V, Barbier N, Calders K, et al. The importance of consistent global forest aboveground biomass product validation. Surveys in geophysics 2019;40:979–999.

[8] Bruggisser M, Hollaus M, Kükenbrink D, Pfeifer N. Comparison of forest structure metrics derived from UAV lidar and ALS data. ISPRS Annals of the Photogrammetry, Remote Sensing and Spatial Information Sciences 2019;4:325–332.

[9] Labrière N, Davies SJ, Disney MI, Duncanson LI, Herold M, Lewis SL, et al. Toward a forest biomass reference measurement system for remote sensing applications. Global Change Biology 2023;29(3):827–840.

[10] Duncanson L, Kellner JR, Armston J, Dubayah R, Minor DM, Hancock S, et al. Aboveground biomass density models for NASA's Global Ecosystem Dynamics Investigation (GEDI) lidar mission. Remote Sensing of Environment 2022;270:112845.

[11] Quegan S, Le Toan T, Chave J, Dall J, Exbrayat JF, Minh DHT, et al. The European Space Agency BIOMASS mission: Measuring forest above-ground biomass from space. Remote Sensing of Environment 2019;227:44–60.

[12] Hyyppä E, Yu X, Kaartinen H, Hakala T, Kukko A, Vastaranta M, et al. Comparison of backpack, handheld, under-canopy UAV, and above-canopy UAV laser scanning for field reference data collection in boreal forests. Remote Sensing 2020;12(20):3327.

[13] Li N, Ho CP, Xue J, Lim LW, Chen G, Fu YH, et al. A Progress Review on Solid-State LiDAR and Nanophotonics-Based LiDAR Sensors. Laser & Photonics Reviews 2022;16(11):2100511.

[14] Xu D, Wang H, Xu W, Luan Z, Xu X. LiDAR applications to estimate forest biomass at individual tree scale: Opportunities, challenges and future perspectives. Forests 2021;12(5):550.

[15] Ferraz A, Saatchi S, Mallet C, Meyer V. Lidar detection of individual tree size in tropical forests. Remote Sensing of Environment 2016;183:318–333.

[16] Brandt M, Tucker CJ, Kariryaa A, Rasmussen K, Abel C, Small J, et al. An unexpectedly large count of trees in the West African Sahara and Sahel. Nature 2020;587(7832):78–82.

[17] Calders K, Adams J, Armston J, Bartholomeus H, Bauwens S, Bentley LP, et al. Terrestrial laser scanning in forest ecology: Expanding the horizon. Remote Sensing of Environment 2020;251:112102.

[18] Demol M, Verbeeck H, Gielen B, Armston J, Burt A, Disney M, et al. Estimating forest above-ground biomass with terrestrial laser scanning: Current status and future directions. Methods in Ecology and Evolution 2022;13(8):1628–1639.

[19] Valbuena R, O'Connor B, Zellweger F, Simonson W, Vihervaara P, Maltamo M, et al. Standardizing ecosystem morphological traits from 3D information sources. Trends in Ecology & Evolution 2020;35(8):656–667.

[20] Hao Z, Lin L, Post CJ, Jiang Y, Li M, Wei N, et al. Assessing tree height and density of a young forest using a consumer unmanned aerial vehicle (UAV). New Forests 2021;52:843–862.

[21] Hyyppä E, Hyyppä J, Hakala T, Kukko A, Wulder MA, White JC, et al. Under-canopy UAV laser scanning for accurate forest field measurements. ISPRS Journal of Photogrammetry and Remote Sensing 2020;164:41–60.

[22] Jin C, Oh Cy, Shin S, Wilfred Njungwi N, Choi C. A comparative study to evaluate accuracy on canopy height and density using UAV, ALS, and fieldwork. Forests 2020;11(2):241.

[23] Machimura T, Fujimoto A, Hayashi K, Takagi H, Sugita S. A novel tree biomass estimation model applying the pipe model theory and adaptable to UAV-derived canopy height models. Forests 2021;12(2):258.

[24] Kruuvcek M, Trochta J, Cibulka M, Kral K. Beyond the cones: How crown shape plasticity alters aboveground competition for space and light—Evidence from terrestrial laser scanning. Agricultural and Forest Meteorology 2019;264:188–199.

[25] Neuville R, Bates JS, Jonard F. Estimating forest structure from UAV-mounted LiDAR point cloud using machine learning. Remote sensing 2021;13(3):352.

[26] Solvin TM, Puliti S, Steffenrem A. Use of UAV photogrammetric data in forest genetic trials: measuring tree height, growth, and phenology in Norway spruce (Picea abies L. Karst.). Scandinavian Journal of Forest Research 2020;35(7):322–333.

[27] Jiang H, Cheng S, Yan G, Kuusk A, Hu R, Tong Y, et al. Clumping Effects in Leaf Area Index Retrieval From Large-Footprint Full-Waveform LiDAR. IEEE Transactions on Geoscience and Remote Sensing 2021;60:1–20.

[28] Yao W, Krull J, Krzystek P, Heurich M. Sensitivity analysis of 3D individual tree detection from LiDAR point clouds of temperate forests. Forests 2014;5(6):1122–1142.

[29] Hao Y, Widagdo FRA, Liu X, Quan Y, Dong L, Li F. Individual tree diameter estimation in small-scale forest inventory using UAV laser scanning. Remote Sensing 2020;13(1):24.

[30] Yang Z, Liu Q, Luo P, Ye Q, Sharma RP, Duan G, et al. Nonlinear mixed-effects height to crown base model based on both airborne LiDAR and field datasets for Picea crassifolia Kom trees in northwest China. Forest Ecology and Management 2020;474:118323.

[31] Liu X, Hao Y, Widagdo FRA, Xie L, Dong L, Li F. Predicting height to crown base of Larix olgensis in Northeast China Using UAV-LiDAR data and nonlinear mixed effects models. Remote Sensing 2021;13(9):1834.

[32] Sun S, Cao QV, Cao T. Evaluation of distance-independent competition indices in predicting tree survival and diameter growth. Canadian Journal of Forest Research 2019;49(5):440–446.

[33] Zhang B, Sajjad S, Chen K, Zhou L, Zhang Y, Yong KK, et al. Predicting tree height-diameter relationship from relative competition levels using quantile regression models for Chinese fir (Cunninghamia lanceolata) in Fujian province, China. Forests 2020;11(2):183.

[34] Lo CS, Lin C. Growth-competition-based stem diameter and volume modeling for tree-level forest inventory using airborne LiDAR data. IEEE Transactions on Geoscience and Remote Sensing 2012;51(4):2216–2226.

[35] Andersen HE, McGaughey RJ, Reutebuch SE. Estimating forest canopy fuel parameters using LIDAR data. Remote sensing of Environment 2005;94(4):441–449.

[36] Næsset E, Økland T. Estimating tree height and tree crown properties using airborne scanning laser in a boreal nature reserve. Remote Sensing of Environment 2002;79(1):105–115.

[37] Rijal B, Weiskittel AR, Kershaw Jr JA. Development of height to crown base models for thirteen tree species of the North American Acadian Region. The Forestry Chronicle 2012;88(1):60–73.

[38] Biging GS, Dobbertin M. Evaluation of competition indices in individual tree growth models. Forest science 1995;41(2):360–377.

[39] Antonio N, Tome M, Tome J, Soares P, Fontes L. Effect of tree, stand, and site variables on the allometry of Eucalyptus globulus tree biomass. Canadian Journal of Forest Research 2007;37(5):895–906.

[40] Silvertown J. Plant coexistence and the niche. Trends in Ecology & evolution 2004;19(11):605–611.

[41] Pachepsky E, Bown JL, Eberst A, Bausenwein U, Millard P, Squire GR, et al. Consequences of intraspecific variation for the structure and function of ecological communities Part 2: Linking diversity and function. Ecological Modelling 2007;207(2-4):277–285.

[42] Liu S, Brandt M, Nord-Larsen T, Chave J, Reiner F, Lang N, et al. The overlooked contribution of trees outside forests to tree cover and woody biomass across Europe. Preprint 2023;.

[43] Anselin L. Local indicators of spatial association—LISA. Geographical analysis 1995;27(2):93–115.

[44] Valladares F, Arrieta S, Aranda I, Lorenzo D, Sánchez-Gómez D, Tena D, et al. Shade tolerance, photoinhibition sensitivity and phenotypic plasticity of Ilex aquifolium in continental Mediterranean sites. Tree physiology 2005;25(8):1041–1052.

[45] Valladares F, Dobarro I, Sánchez-Gomez D, Pearcy RW. Photoinhibition and drought in Mediterranean woody saplings: scaling effects and interactions in sun and shade phenotypes. Journal of Experimental Botany 2005;56(411):483–494.

[46] Goebes P, Schmidt K, Seitz S, Both S, Bruelheide H, Erfmeier A, et al. The strength of soil-plant interactions under forest is related to a Critical Soil Depth. Scientific Reports 2019;9(1):8635.

[47] Green JK, Keenan TF. The limits of forest carbon sequestration. Science 2022;376(6594):692–693.

[48] Anselin L, Rey SJ. Perspectives on spatial data analysis. In: Perspectives on spatial data analysis Springer; 2010.p. 1–20.

[49] Valladares F, Gianoli E, Gómez JM. Ecological limits to plant phenotypic plasticity. New phytologist 2007;176(4):749–763.

[50] Schiefer F, Kattenborn T, Frick A, Frey J, Schall P, Koch B, et al. Mapping forest tree species in high resolution UAV-based RGB-imagery by means of convolutional neural networks. ISPRS Journal of Photogrammetry and Remote Sensing 2020;170:205–215.

[51] Marques O, Barenholtz E, Charvillat V. Context modeling in computer vision: techniques, implications, and applications. Multimedia Tools and Applications 2011;51:303–339.

[52] Zhao R, Ouyang W, Li H, Wang X. Saliency Detection by Multi-Context Deep Learning. In: Proceedings of the IEEE Conference on Computer Vision and Pattern Recognition (CVPR); 2015. p. 1265–1274.

[53] Luo W, Li Y, Urtasun R, Zemel R. Understanding the effective receptive field in deep convolutional neural networks. Advances in neural information processing systems 2016;29.

[54] Yang W, Tan RT, Feng J, Liu J, Guo Z, Yan S. Deep joint rain detection and removal from a single image. In: Proceedings of the IEEE conference on computer vision and pattern recognition; 2017. p. 1357–1366.

[55] Liu YF, Jaw DW, Huang SC, Hwang JN. DesnowNet: Context-aware deep network for snow removal. IEEE Transactions on Image Processing 2018;27(6):3064–3073.

[56] Chu HJ, Wu CF, Lin YP. Incorporating spatial autocorrelation with neural networks in empirical land-use change models. Environment and Planning B: Planning and Design 2013;40(3):384–404.

[57] Reichstein M, Camps-Valls G, Stevens B, Jung M, Denzler J, Carvalhais N. Deep learning and process understanding for data-driven Earth system science. Nature 2019;566(7743):195–204.

[58] Chakraborti S, Das DN, Mondal B, Shafizadeh-Moghadam H, Feng Y. A neural network and landscape metrics to propose a flexible urban growth boundary: A case study. Ecological indicators 2018;93:952–965.

[59] Heiskanen J, C B, N B, C C, H C, B G, et al. The Integrated Carbon Observation System in Europe. Bulletin of the American Meteorological Society 2022;103(3):E855–E872.

[60] WSL, Long-term Forest Ecosystem Research (WSL); 2023. https://www.wsl.ch/en/about-wsl/organisation/programmes-and-initiatives/.

[61] TreeNet, Biological drought and growth indicator network; 2023. https://treenet.info/.

[62] ETH-Zurich, Biological drought and growth indicator network; 2023. https://www.swissfluxnet.ethz.ch/.

[63] ICOS, Integrated Carbon Observation System; 2023. https://www.icos-cp.eu/.

[64] ICP-Forest, International Co-operative Programme on Assessment and Monitoring of Air Pollution Effects on Forests; 2023. http://icp-forests.net/.

[65] eLTER, Integrated European Long-Term Ecosystem, critical zone and socio-ecological Research; 2023. https://elter-ri.eu/.

[66] Revenga JC, Trepekli K, Oehmcke S, Jensen R, Li L, Igel C, et al. Above-Ground Biomass Prediction for Croplands at a Sub-Meter Resolution Using UAV–LiDAR and Machine Learning Methods. Remote Sensing 2022;14(16):3912.

[67] Davidson L, Mills J, Haynes I, Augarde C, Bryan P, Douglas M. Airborne to UAS LiDAR: An analysis of UAS LiDAR ground control targets. ISPRS Geospatial Week 2019;.

[68] Swiss Federal Institute for Forest S, (WSL) LR, Methods of the Sanasilva Inventory; 2023. https://www.wsl.ch/en/forest/forest-development-and-monitoring/sanasilva-forest-health-inventory/methods-of-the-sanasilva-inventory.html.

[69] Hunziker S, Begert M, Scherrer SC, Rigling A, Gessler A. Below average midsummer to early autumn precipitation evolved into the main driver of sudden Scots pine vitality decline in the Swiss Rhône valley. Frontiers in Forests and Global Change 2022;p. 103.

[70] http://www icos-etc eu/icos/documents/instructions/ancfor, Instruction on ancillary vegetation measurements in forest; 2023. http://www.icos-etc.eu/icos/documents/instructions/ancfor.

[71] Chen Q GP Baldocchi D, M K. Isolating Individual Trees in a Savanna Woodland Using Small Footprint Lidar Data. In: Photogrammetric Engineering and Remote Sensing, 72(8): 923-932; 2006. p. 923–932.

[72] International G. LiDAR360 User Guide. California, USA; January 2021, www.greenvalleyintl.com.

[73] Breunig MM, Kriegel HP, Ng RT, Sander J. LOF: identifying density-based local outliers. In: Proceedings of the 2000 ACM SIGMOD international conference on Management of data; 2000. p. 93–104.

[74] Liu FT, Ting KM, Zhou ZH. Isolation forest. In: 2008 eighth ieee international conference on data mining IEEE; 2008. p. 413–422.

[75] Anselin L, Syabri I, Kho Y. GeoDa: an introduction to spatial data analysis. In: Handbook of applied spatial analysis: Software tools, methods and applications Springer; 2009.p. 73–89.

[76] Da Silva BC, Basso EW, Bazzan AL, Engel PM. Dealing with non-stationary environments using context detection. In: Proceedings of the 23rd international conference on Machine learning; 2006. p. 217–224.

[77] Cressie N. Statistics for spatial data. John Wiley & Sons; 2015.

[78] Getis A, Ord JK. The analysis of spatial association by use of distance statistics. In: Perspectives on spatial data analysis Springer; 2010.p. 127–145.

[79] Westerholt R, Resch B, Mocnik FB, Hoffmeister D. A statistical test on the local effects of spatially structured variance. International Journal of Geographical Information Science 2018;32(3):571–600.

[80] Hastie TJ. Generalized additive models. In: Statistical models in S Routledge; 2017.p. 249–307.

[81] Anselin L, et al. Spatial econometrics. A companion to theoretical econometrics 2001;310330.

[82] Beven KJ, Kirkby MJ. A physically based, variable contributing area model of basin hydrology/Un modèle à base physique de zone d'appel variable de l'hydrologie du bassin versant. Hydrological sciences journal 1979;24(1):43–69.

[83] Kopeckỳ M, Macek M, Wild J. Topographic Wetness Index calculation guidelines based on measured soil moisture and plant species composition. Science of the Total Environment 2021;757:143785.

[84] Institute ESR. ArcGis Pro: Implementation Guide. Redlands, California; 2021, www.esri.com.

[85] Landini G, Particles8 class: An ImageJ plugin for estimating various statistics of binary 8- connected particles.; 2010. https://blog.bham.ac.uk/intellimic/g-landini-software, accessed on November 25, 2022.

[86] Güler C, Beyhan B, Tağa H. PolyMorph-2D: An open-source GIS plug-in for morphometric analysis of vector-based 2D polygon features. Geomorphology 2021;386:107755.

[87] Steiniger S, Blake L, OpenJUMP;. www.openjump.org.

[88] Freund Y, Schapire RE. A decision-theoretic generalization of on-line learning and an application to boosting. Journal of computer and system sciences 1997;55(1):119–139.

[89] Friedman JH. Greedy function approximation: a gradient boosting machine. Annals of statistics 2001;p. 1189–1232.

[90] Tibshirani R. Regression shrinkage and selection via the lasso. Journal of the Royal Statistical Society: Series B (Methodological) 1996;58(1):267–288.

[91] Ho TK. Random decision forests. In: Proceedings of 3rd international conference on document analysis and recognition, vol. 1 IEEE; 1995. p. 278–282.

[92] Schapire RE. Explaining adaboost. Empirical Inference: Festschrift in Honor of Vladimir N Vapnik 2013;p. 37–52.

[93] Vidaurre D, Bielza C, Larranaga P. A survey of L1 regression. International Statistical Review 2013;81(3):361–387.

[94] Dalponte M, Coomes DA. Tree-centric mapping of forest carbon density from airborne laser scanning and hyperspectral data. Methods in ecology and evolution 2016;7(10):1236–1245.

[95] Gryc V, Horáček P. Variability in density of spruce (Picea abies [L.] Karst.) wood with the presence of reaction wood. Journal of forest science 2007;53(3):129–137.

[96] Scrinzi G, Galvagni D, Marzullo L. I nuovi modelli dendrometrici per la stima delle masse assestamentali in Provincia di Trento. Provincia autonoma di Trento. Servizio foreste e fauna; 2010.

[97] Quionero-Candela J, Sugiyama M, Schwaighofer A, Lawrence ND. Data Set Shift in Machine Learning. MIT Press, Cambridge, Massachusetts; 2009. http://www.acad.bg/ebook/ml/The.MIT.Press.Dataset.Shift.in.Machine.Learning.Feb.2009.eBook-DDU.pdf.

[98] Bates S, Hastie T, Tibshirani R. Cross-validation: what does it estimate and how well does it do it? arXiv preprint arXiv:210400673 2021;.

[99] Wilcoxon F. Individual comparisons by ranking methods. Springer; 1992.

[100] Cliff N. Dominance statistics: Ordinal analyses to answer ordinal questions. Psychological bulletin 1993;114(3):494.

[101] Fu WJ, Jiang PK, Zhou GM, Zhao KL. Using Moran's I and GIS to study the spatial pattern of forest litter carbon density in a subtropical region of southeastern China. Biogeosciences 2014;11(8):2401–2409.

[102] Horton RE. Drainage-basin characteristics. Transactions, American geophysical union 1932;13(1):350–361.

[103] Zingg T. Beitrag zur schotteranalyse. PhD thesis, ETH Zurich; 1935.

[104] Buendıa P, Soler C, Paolicchi F, Gago G, Urquieta B, Pérez-Sánchez F, et al. Morphometric characterization and classification of alpaca sperm heads using the Sperm-Class Analyzer® computer-assisted system. Theriogenology 2002;57(4):1207–1218.

[105] Attneave F, Arnoult MD. The quantitative study of shape and pattern perception. Psychological bulletin 1956;53(6):452.

[106] Zăvoianu I. Morfometria bazinelor hidrografice. Editura Academiei Republicii Socialiste România; 1978.

[107] Miller VC. A QUANTITATIVE GEOMORPHIC STUDY OF DRAINAGE BASIN CHARACTERISTICS IN THE CLINCH MOUNTAIN AREA VIRGINIA AND TENNESSEE. Columbia Univ New York; 1953.

[108] Schumm SA. Evolution of drainage systems and slopes in badlands at Perth Amboy, New Jersey. Geological society of America bulletin 1956;67(5):597–646.

[109] Chorley RJ, Malm E Donald E, Pogorzelski HA. A new standard for estmating drainage basin shape. American Journal of Science 1957;255:138–141.

[110] Horgan GW, Glasbey CA. Uses of digital image analysis in electrophoresis. Electrophoresis 1995;16(1):298–305.

[111] Zunic J, Rosin PL. A new convexity measure for polygons. IEEE Transactions on Pattern Analysis and Machine Intelligence 2004;26(7):923–934.

[112] Rosin PL. Measuring rectangularity. Machine Vision and Applications 1999;11:191–196.

[113] Wadell H. Volume, shape, and roundness of quartz particles. The Journal of Geology 1935;43(3):250–280.

[114] Altmann A, Toloşi L, Sander O, Lengauer T. Permutation importance: a corrected feature importance measure. Bioinformatics 2010;26(10):1340–1347.

[115] Pillar VD, Duarte LdS, Sosinski EE, Joner F. Discriminating trait-convergence and trait-divergence assembly patterns in ecological community gradients. Journal of Vegetation Science 2009;20(2):334–348.

[116] Guillén-Escribà C, Schneider FD, Schmid B, Tedder A, Morsdorf F, Furrer R, et al. Remotely sensed between-individual functional trait variation in a temperate forest. Ecology and Evolution 2021;11(16):10834–10867.

[117] Zheng Z, Zeng Y, Schuman MC, Jiang H, Schmid B, Schaepman ME, et al. Individual tree-based vs pixel-based approaches to mapping forest functional traits and diversity by remote sensing. International Journal of Applied Earth Observation and Geoinformation 2022;114:103074.

[118] Ma X, Migliavacca M, Wirth C, Bohn FJ, Huth A, Richter R, et al. Monitoring plant functional diversity using the reflectance and echo from space. Remote Sensing 2020;12(8):1248.

[119] He X, Zemel RS, Carreira-Perpinán MA. Multiscale conditional random fields for image labeling. In: Proceedings of the 2004 IEEE Computer Society Conference on Computer Vision and Pattern Recognition, 2004. CVPR 2004., vol. 2 IEEE; 2004. p. II–II.

[120] Yu F, Koltun V. Multi-scale context aggregation by dilated convolutions. arXiv preprint arXiv:151107122 2015;.

[121] Abelleira Martínez OJ, Fremier AK, Günter S, Ramos Bendaña Z, Vierling L, Galbraith SM, et al. Scaling up functional traits for ecosystem services with remote sensing: concepts and methods. Ecology and Evolution 2016;6(13):4359–4371.

[122] Kraft NJ, Adler PB, Godoy O, James EC, Fuller S, Levine JM. Community assembly, coexistence and the environmental filtering metaphor. Functional ecology 2015;29(5):592–599.

[123] Berrar D, Cross-Validation.; 2019.

[124] Cooper HF, Grady KC, Cowan JA, Best RJ, Allan GJ, Whitham TG. Genotypic variation in phenological plasticity: Reciprocal common gardens reveal adaptive responses to warmer springs but not to fall frost. Global change biology 2019;25(1):187–200.

[125] Ludovisi R, Tauro F, Salvati R, Khoury S, Mugnozza Scarascia G, Harfouche A. UAV-based thermal imaging for high-throughput field phenotyping of black poplar response to drought. Frontiers in plant science 2017;8:1681.

[126] Rallo P, de Castro AI, López-Granados F, Morales-Sillero A, Torres-Sánchez J, Jiménez MR, et al. Exploring UAV-imagery to support genotype selection in olive breeding programs. Scientia Horticulturae 2020;273:109615.

[127] Sankey T, Hultine K, Blasini D, Koepke D, Bransky N, Grady K, et al. UAV thermal image detects genetic trait differences among populations and genotypes of Fremont cottonwood (Populus fremontii, Salicaceae). Remote Sensing in Ecology and Conservation 2021;7(2):245–258.

[128] Fahey RT, Atkins JW, Gough CM, Hardiman BS, Nave LE, Tallant JM, et al. Defining a spectrum of integrative trait-based vegetation canopy structural types. Ecology letters 2019;22(12):2049–2059.

[129] Qu Y, Mo S, Niu J. Dat: Training deep networks robust to label-noise by matching the feature distributions. In: Proceedings of the IEEE/CVF Conference on Computer Vision and Pattern Recognition; 2021. p. 6821–6829.

[130] Dubayah R, Luthcke S, Sabaka T, Nicholas J, Preaux S, Hofton M, GEDI L3 Gridded Land Surface Metrics. Version; 2021.

[131] Horton RE. Erosional development of streams and their drainage basins; hydrophysical approach to quantitative morphology. Geological society of America bulletin 1945;56(3):275–370.

[132] Strahler AN. Hypsometric (area-altitude) analysis of erosional topography. Geological society of America bulletin 1952;63(11):1117–1142.